

BOUNDS ON REPRESENTATION-INDUCED CONFOUNDING BIAS FOR TREATMENT EFFECT ESTIMATION

Valentyn Melnychuk, Dennis Frauen & Stefan Feuerriegel

LMU Munich & Munich Center for Machine Learning

Munich, Germany

melnychuk@lmu.de

ABSTRACT

State-of-the-art methods for conditional average treatment effect (CATE) estimation make widespread use of representation learning. Here, the idea is to reduce the variance of the low-sample CATE estimation by a (potentially constrained) low-dimensional representation. However, low-dimensional representations can lose information about the observed confounders and thus lead to bias, because of which the validity of representation learning for CATE estimation is typically violated. In this paper, we propose a new, representation-agnostic refutation framework for estimating bounds on the *representation-induced confounding bias* that comes from dimensionality reduction (or other constraints on the representations) in CATE estimation. First, we establish theoretically under which conditions CATE is non-identifiable given low-dimensional (constrained) representations. Second, as our remedy, we propose a neural refutation framework which performs partial identification of CATE or, equivalently, aims at estimating lower and upper bounds of the representation-induced confounding bias. We demonstrate the effectiveness of our bounds in a series of experiments. In sum, our refutation framework is of direct relevance in practice where the validity of CATE estimation is of importance.

1 INTRODUCTION

Estimating conditional average treatment effect (CATE) from observational data is important for many applications in medicine (Kraus et al., 2023; Feuerriegel et al., 2024), marketing (Varian, 2016), and economics (Imbens & Angrist, 1994). For example, medical professionals use electronic health records to personalize care based on the estimated CATE.

Different machine learning methods have been developed for CATE estimation (see Sec. 2 for an overview). In this paper, we focus on representation learning methods (e.g., Johansson et al., 2016; Shalit et al., 2017; Hassanpour & Greiner, 2019b;a; Zhang et al., 2020; Assaad et al., 2021; Johansson et al., 2022). Representation learning methods have several benefits: (1) They often achieve state-of-the-art performance, especially in low-sample regimens. (2) They provide generalization bounds for best-in-class estimation, regardless of whether ground-truth CATE belongs to a specified model class. (3) They manage to reduce the variance of the low-sample CATE estimation by using a (potentially constrained) low-dimensional representation. Often, constraints are imposed on the representations such as balancing with an empirical probability metric and invertibility.

While representation learning methods benefit from reducing variance, they also have a shortcoming: low-dimensional (potentially constrained) representations can lose information about covariates, including information about ground-truth confounders. As we show later, such low-dimensional representations can thus lead to bias, because of which the validity of representation learning methods may be violated. To this end, we introduce the notion of *representation-induced confounding bias* (RICB). As a result of the RIBC, the validity of representation learning for CATE estimation is typically violated, and we thus offer remedies in our paper.

In this paper, we propose a new, representation-agnostic refutation framework for estimating bounds on the RIBC that comes from dimensionality reduction (or other constraints on the representation). First, we show in which settings CATE is non-identifiable due to the RIBC. We further discuss how

Table 1: Overview of key representation learning methods for CATE estimation.

Method	Invertibility	Balancing with	
		empirical probability metrics	loss re-weighting
TARNet (Shalit et al., 2017; Johansson et al., 2022)	–	–	–
BNN (Johansson et al., 2016); CFR (Shalit et al., 2017; Johansson et al., 2022); ESCFR (Wang et al., 2024)	–	IPM (MMD, WM)	–
RCFR (Johansson et al., 2018; 2022)	–	IPM (MMD, WM)	Learnable weights
DACPOL (Atan et al., 2018); CRN (Bica et al., 2020); ABCEI (Du et al., 2021); CT (Melnichuk et al., 2022); MitNet (Guo et al., 2023); BNCDE (Hess et al., 2024)	–	JSD (adversarial learning)	–
SITE (Yao et al., 2018)	Local similarity	Middle point distance	–
CFR-ISW (Hassanpour & Greiner, 2019a); DR-CFR (Hassanpour & Greiner, 2019b); DeR-CFR (Wu et al., 2022)	–	IPM (MMD, WM)	Representation propensity
DKLITE (Zhang et al., 2020)	Reconstruction loss	Counterfactual variance	–
BWCFR (Assaad et al., 2021)	–	IPM (MMD, WM)	Covariate propensity
PM (Schwab et al., 2018); StableCFR (Wu et al., 2023)	–	–	Upsampling via matching

IPM: integral probability metric; MMD: maximum mean discrepancy; WM: Wasserstein metric; JSD: Jensen-Shannon divergence

different constraints imposed on the representation impact the RICB. Then, as a remedy, we perform partial identification of CATE or, equivalently, estimate lower and upper bounds on the RICB.

We empirically demonstrate the effectiveness of our refutation framework on top of many state-of-the-art representation learning methods for CATE estimation. We thereby show that the established representation learning methods for CATE estimation such as BNN (Johansson et al., 2016); TARNet, CFR, RCFR (Shalit et al., 2017; Johansson et al., 2018; 2022); CFR-ISW (Hassanpour & Greiner, 2019a); and BWCFR (Assaad et al., 2021) can be more reliable for decision-making when combined with our refutation framework. We thus evaluate decision-making based on CATE, finding that the policies with deferral that account for our bounds on the RICB achieve lower error rates than the decisions based on CATE estimates from the original representation learning method. As such, our refutation framework offers a tool for practitioners to check the validity of CATE estimates from representation learning methods and further improve the reliability and safety of representation learning in CATE estimation.

In sum, our **contributions** are following:¹ (1) We show that the CATE from representation learning methods can be non-identifiable due to a *representation-induced confounding bias*. To the best of our knowledge, we are the first to formalize such bias. (2) We propose a representation-agnostic refutation framework to perform partial identification of CATE, so that we estimate lower and upper bounds of the representation-induced confounding bias. (3) We demonstrate the effectiveness of our bounds together with a wide range of state-of-the-art CATE methods.

2 RELATED WORK

An extensive body of literature has focused on CATE estimation. We provide an extended overview in Appendix A, while, in the following, we focus on two important streams relevant to our framework.

Representation learning for CATE estimation. Seminal works of Johansson et al. (2016); Shalit et al. (2017); and Johansson et al. (2022) provided generalization bounds for representation learning methods aimed at CATE estimation under the assumption of *invertibility* of the representations. Therein, the authors demonstrated, that generalization bounds depend on the imbalance of the invertible representations between treated and untreated subgroups, and some form of *balancing* is beneficial for reducing the variance. However, although invertibility of representations is still required theoretically, it is usually not enforced in practice (see Table 1). Namely, due to bias-variance trade-off, low-dimensional (non-invertible) representations can still generalize better, although potentially containing confounding bias (Ding et al., 2017).

Numerous works offer a variety of tailored deep representation learning methods for CATE estimation by extending TARNet (Shalit et al., 2017; Johansson et al., 2022) (the simplest representation leaning CATE estimator) with different ways to enforce (i) invertibility and (ii) balancing. For example, (i) invertibility was enforced via local similarity in SITE (Yao et al., 2018), and via reconstruction loss in DKLITE (Zhang et al., 2020). (ii) Balancing was implemented as both (1) a constraint on the representation with some empirical probability metric and (2) loss re-weighting. Examples of (1) include balancing with *integral probability metrics* in, e. g., BNN (Johansson et al., 2016), and CFR (Shalit et al., 2017; Johansson et al., 2022); *Jensen-Shannon divergence* in, e. g., DACPOL (Atan et al., 2018), CT (Melnichuk et al., 2022), and MitNet (Guo et al., 2023); *middle point distance*

¹Code is available at <https://github.com/Valentyn1997/RICB>.

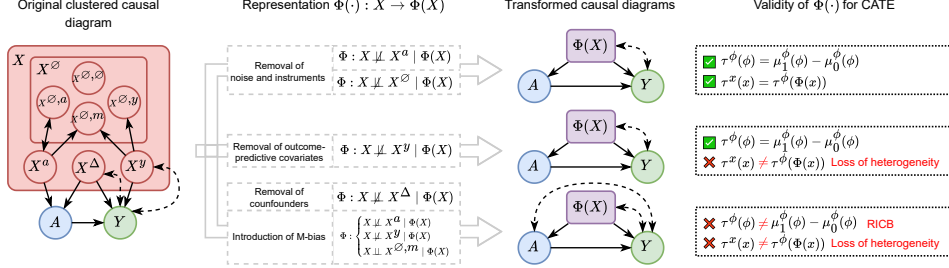


Figure 1: The validity of CATE estimation is influenced by the different constraints imposed on representations $\Phi(\cdot)$. In red: different violations of valid CATE estimation.

in SITE (Yao et al., 2018); and *counterfactual variance* in DKLITE (Zhang et al., 2020). (2) Loss re-weighting was implemented with *learnable weights* in RCFR (Johansson et al., 2018; 2022); *inverse propensity weights* in, e. g., CFR-ISW (Hassanpour & Greiner, 2019a) and BWCFR (Assaad et al., 2021); and *upsampling* in PM (Schwab et al., 2018) and StableCFR (Wu et al., 2023). We provide the full overview of key representation learning methods for CATE in Table 1.

Handling unobserved confounding. Sensitivity models are used to estimate the bias in treatment effect estimation due to the *hidden confounding* by limiting the strength of hidden confounding through a sensitivity parameter. There are two main classes of sensitivity models: outcome sensitivity models (OSMs) (Robins et al., 2000; Blackwell, 2014; Bonvini et al., 2022) and propensity (marginal) sensitivity models (MSMs) (Tan, 2006; Jesson et al., 2021; Bonvini et al., 2022; Dorn & Guo, 2022; Frauen et al., 2023; Oprescu et al., 2023). We later adopt ideas from the MSMs to derive our refutation framework, because they only require knowledge of propensity scores wrt. covariates and representation, but *not* the actual expected potential outcomes as required by OSMs.

Of note, our method uses MSMs but in an unconventional way. Importantly, we do not use MSMs for sensitive analysis but for partial identification. As such, we do *not* face the common limitation of MSMs in that the sensitivity parameter (which guides the amount of hidden confounding) must be chosen through expert knowledge. In contrast, our application allows us to estimate the sensitivity parameters in the MSM from data.

Research gap: To the best of our knowledge, no work has studied the confounding bias in low-dimensional (constrained) representations for CATE estimation. Our novelty is to formalize the *representation-induced confounding bias* and to propose a neural refutation framework for estimating bounds.

3 VALIDITY OF REPRESENTATION LEARNING FOR CATE

In the following, we first formalize representation learning for CATE estimation (Sec. 3.1). We then define the concept of valid representations and give two conditions when this is violated (Sec. 3.2). Finally, we lay out the implications of invalid representations (Sec. 3.3).

Notation. Let X be a random variable with a realization x , distribution $\mathbb{P}(X)$, density/probability function $\mathbb{P}(X = x)$ and domain \mathcal{X} , respectively. Furthermore, let $\mathbb{P}(Y | X = x, A = a)$ be the conditional distribution of the outcome Y . Let $\pi_a^x(x) = \mathbb{P}(A = a | X = x)$ denote the covariate propensity score for treatment A and covariates X , and $\mu_a^x(x) = \mathbb{E}(Y | A = a, X = x)$ an expected covariate-conditional outcome. Analogously, $\pi_a^\phi(\phi) = \mathbb{P}(A = a | \Phi(X) = \phi)$ and $\mu_a^\phi(\phi) = \mathbb{E}(Y | A = a, \Phi(X) = \phi)$ are the representation propensity score and the expected representation-conditional outcome, respectively, for treatment A and representation $\Phi(X)$. Importantly, in the definitions of π_a^x , μ_a^x , π_a^ϕ , and μ_a^ϕ , upper indices serve as indicators that the nuisance functions relate either to the covariates or to the representations and, therefore, are not arguments. Let $Y[a]$ denote a potential outcome after intervening on the treatment $do(A = a)$. $\text{dist}[\cdot]$ is some distributional distance.

3.1 REPRESENTATION LEARNING FOR CATE

Problem setup. Assume we have observational data \mathcal{D} with a binary treatment $A \in \{0, 1\}$, high-dimensional covariates $X \in \mathcal{X} \subseteq \mathbb{R}^{d_x}$, and a continuous outcome $Y \in \mathcal{Y} \subseteq \mathbb{R}$. In medicine, A could be ventilation, X the patient’s health history, and Y respiratory rate.

Without a loss of generality, we assume that covariates X are an implicit cluster (Anand et al., 2023) of four sub-covariates, $X = \{X^\emptyset, X^a, X^y, X^\Delta\}$, namely, (1) noise, (2) instruments, (3) outcome-predictive covariates, and (4) confounders (Cinelli et al., 2022) (see clustered causal diagram in Fig. 1). The noise, in turn, can be partitioned onto (1.1) an independent noise, (1.2) descendants of instruments, (1.3) descendants of outcome-predictive covariates, and (1.4) M-bias-inducing covariates, namely, $X^\emptyset = \{X^{\emptyset,\emptyset}, X^{\emptyset,a}, X^{\emptyset,y}, X^{\emptyset,m}\}$. Importantly, some sub-covariates could be empty, and the partitioning of X is usually unknown in practice, and, thus, it will be only used in this paper to provide better intuition (all experiments later consider the partitioning as unknown). The observational data are sampled i.i.d. from a joint distribution, i. e., $\mathcal{D} = \{x_i, a_i, y_i\}_{i=1}^n \sim \mathbb{P}(X, A, Y)$, where n is the sample size. Furthermore, potential outcomes are only observed for factual treatments, i. e., $Y = AY[1] + (1 - A)Y[0]$, which is referred as the fundamental problem of causal inference.

The *conditional average treatment effect* (CATE) is then defined as

$$\tau^x(x) = \mathbb{E}(Y[1] - Y[0] \mid X = x), \quad (1)$$

where upper index τ indicates that CATE is with respect to the covariates x . Identification of CATE from observational data relies on Neyman–Rubin potential outcomes framework (Rubin, 1974). As such, we assume (i) *consistency*: if $A = a$ then $Y = Y[a]$; (ii) *overlap*: $\mathbb{P}(0 < \pi_a^x(X) < 1) = 1$; and (iii) *exchangeability*: $A \perp\!\!\!\perp (Y[0], Y[1]) \mid X$. Under assumptions (i)–(iii), the CATE is **identifiable** from observational data, $\mathbb{P}(X, A, Y)$, i. e. from expected covariate-conditional outcomes, $\tau^x(x) = \mu_1^x(x) - \mu_0^x(x)$.

Representation learning for CATE estimation. Representations learning methods CATE estimators (Johansson et al., 2016; Shalit et al., 2017; Johansson et al., 2022) do not assume a specific partitioning of covariates X and generally consist of two main components: (1) the *representation subnetwork* $\Phi(\cdot)$ and (2) the *potential outcomes predicting subnetwork(s)*, i. e., $f_0(\cdot), f_1(\cdot)$.² Both components are as follows. (1) The representation subnetwork maps all the covariates $X \rightarrow \Phi(X)$ to a low- or equal-dimensional representation space with some measurable function, $\Phi(\cdot) : \mathbb{R}^{d_x} \rightarrow \mathbb{R}^{d_\phi}, d_\phi \leq d_x$.³ Additional constraints can be imposed on $\Phi(\cdot)$. For example, balancing with an empirical probability metric, $\text{dist}[\mathbb{P}(\Phi(X) \mid A = 0), \mathbb{P}(\Phi(X) \mid A = 1)] \approx 0$, and invertibility, $\Phi^{-1}(\Phi(X)) \approx X$. (2) The potential outcomes predicting subnetwork(s) then aim at estimating CATE with respect to the representations, namely

$$\tau^\phi(\phi) = \mathbb{E}(Y[1] - Y[0] \mid \Phi(X) = \phi), \quad (2)$$

where $\phi = \Phi(x)$. Yet, f_0 and f_1 can only access representation-conditional outcomes, and, therefore, instead, estimate $\mu_0^\phi(\phi)$ and $\mu_1^\phi(\phi)$, respectively.

3.2 VALID REPRESENTATIONS

In the following, we discuss under what conditions representations $\Phi(\cdot)$ are valid for CATE estimation, namely, do not introduce an infinite-data bias.

Definition 1 (Valid representations). *We call a representation $\Phi(\cdot)$ valid for CATE if it satisfies the following two equalities:*

$$\tau^x(x) \stackrel{(i)}{=} \tau^\phi(\Phi(x)) \quad \text{and} \quad \tau^\phi(\phi) \stackrel{(ii)}{=} \mu_1^\phi(\phi) - \mu_0^\phi(\phi), \quad (3)$$

where $\tau^x(\cdot)$ and $\tau^\phi(\cdot)$ are CATEs wrt. covariates and representations from Eq. (1) and (2), respectively.

If equality (i) is violated, then we say that the representation suffers from a *loss in heterogeneity*. If (ii) is violated, it suffers from a *representation-induced confounding bias*. Hence, if any of the two is violated, we have invalid representations (see Fig. 1, left).

Characterization of valid representations. We now give two examples of valid representations based on whether information about some sub-covariates $\{X^\emptyset, X^a, X^y, X^\Delta\}$ is fully preserved in $\Phi(X)$.

²The latter can have either one subnetwork with two outputs (SNet) as in, e. g., BNN (Johansson et al., 2016); or two subnetworks (TNet) as in, e. g., TARNet (Shalit et al., 2017).

³The transformation $\Phi(\cdot)$ can also be seen as a mapping between micro-level covariates X to low-dimensional macro-level representations (Rubenstein et al., 2017).

■ *Invertible representations.* A trivial example of a valid representation is an invertible representation (Shalit et al., 2017; Zhang et al., 2020; Johansson et al., 2022):

$$\begin{aligned}\tau^x(x) &\stackrel{(i)}{=} \mathbb{E}(Y[1] - Y[0] \mid X = \Phi^{-1}(\Phi(x))) = \mathbb{E}(Y[1] - Y[0] \mid \Phi(X) = \Phi(x)) = \tau^\phi(\Phi(x)), \\ \tau^x(x) &\stackrel{(ii)}{=} \mathbb{E}(Y \mid A = 1, X = \Phi^{-1}(\Phi(x))) - \mathbb{E}(Y \mid A = 0, X = \Phi^{-1}(\Phi(x))) = \mu_1^\phi(\Phi(x)) - \mu_0^\phi(\Phi(x)),\end{aligned}$$

where equality (ii) follows from setting $\Phi(x)$ to ϕ . Notably, if $\Phi(\cdot)$ is an invertible transformation, then

$$X \perp\!\!\!\perp X^\varnothing \mid \Phi(X), \quad X \perp\!\!\!\perp X^a \mid \Phi(X), \quad X \perp\!\!\!\perp X^y \mid \Phi(X), \quad X \perp\!\!\!\perp X^\Delta \mid \Phi(X), \quad (4)$$

i. e., there is no loss of information on each of the sub-covariates. Eq. (4) holds, as conditioning on $\Phi(X)$ renders each sub-covariate deterministic, thus implying independence. In Lemma 1 of Appendix B, we also show that the opposite statement is true: when all the statements hold in Eq. (4), then $\Phi(\cdot)$ is an invertible transformation.

■ *Removal of noise and instruments.* Another class of valid representations are those, which lose any amount of information about the noise, X^\varnothing , or the instruments, X^a :

$$X \not\perp\!\!\!\perp X^\varnothing \mid \Phi(X) \quad \text{or} \quad X \not\perp\!\!\!\perp X^a \mid \Phi(X). \quad (5)$$

The validity follows from the d-separation in the clustered causal diagram (Fig. 1) and invertibility of $\Phi(\cdot)$ wrt. X^Δ and X^y (see Lemma 2 in Appendix B):

$$\begin{aligned}\tau^x(x) &\stackrel{(i)}{=} \mathbb{E}(Y[1] - Y[0] \mid x) = \mathbb{E}(Y[1] - Y[0] \mid x^\Delta, x^y) = \mathbb{E}(Y[1] - Y[0] \mid \Phi(x)) = \tau^\phi(\Phi(x)), \\ \tau^x(x) &\stackrel{(ii)}{=} \mathbb{E}(Y \mid A = 1, x^\Delta, x^y) - \mathbb{E}(Y \mid A = 0, x^\Delta, x^y) \\ &= \mathbb{E}(Y \mid A = 1, \Phi(x)) - \mathbb{E}(Y \mid A = 0, \Phi(x)) = \mu_1^\phi(\Phi(x)) - \mu_0^\phi(\Phi(x)),\end{aligned} \quad (6)$$

where equality (ii) follows from setting $\Phi(x)$ to ϕ .

In actual implementations, representation learning methods for CATE achieve (1) the loss of information about the instruments through balancing with an empirical probability metric, and (2) the loss of information about the noise by lowering the representation size (which is enforced with the factual outcome loss).

3.3 IMPLICATIONS OF INVALID REPRESENTATIONS

In the following, we discuss the implications for CATE estimation from (1) loss of heterogeneity and (2) RICB for CATE estimation, and in what scenarios they appear in low-dimensional or balanced representations.

(i) **Loss of heterogeneity.** The loss of heterogeneity happens whenever $\tau^x(x) \neq \tau^\phi(\Phi(x))$. It means that the treatment effect at the covariate (individual) level is different from the treatment effect at the representation (aggregated) level. As an example, such discrepancy can occur due to aggregation such as a one-dimensional representation (e.g., as in the covariate propensity score, $\Phi(X) = \pi_1^x(X)$). In this case, the treatment effect $\tau^\phi(\phi)$ denotes a propensity conditional average treatment effect, which is used in propensity matching.

The loss of heterogeneity happens whenever some information about X^Δ or X^y is lost in the representation, i. e.,

$$X \not\perp\!\!\!\perp X^\Delta \mid \Phi(X) \quad \text{or} \quad X \not\perp\!\!\!\perp X^y \mid \Phi(X). \quad (7)$$

This could be the case due to a too low dimensionality of the representation so that the information on X^y or X^Δ is lost, or due to too large balancing with an empirical probability metric so that we lose X^Δ . Then, the equality (i) does not any longer hold in Eq. (3), i. e.,

$$\begin{aligned}\tau^\phi(\Phi(x)) &\stackrel{(i)}{=} \mathbb{E}(Y[1] - Y[0] \mid \Phi(x)) = \int_{\mathcal{X}_\Delta \times \mathcal{X}_Y} \mathbb{E}(Y[1] - Y[0] \mid \Phi(x), x^\Delta, x^y) \mathbb{P}(X^\Delta = x^\Delta, X^y = x^y \mid \Phi(x)) dx^\Delta dx^y \\ &= \int_{\mathcal{X}_\Delta \times \mathcal{X}_Y} \tau^x(x) \mathbb{P}(X^\Delta = x^\Delta, X^y = x^y \mid \Phi(x)) dx^\Delta dx^y \neq \tau^x(x).\end{aligned}$$

Although the CATE wrt. representations, $\tau^\phi(\phi)$, and the CATE wrt. covariates, $\tau^x(x)$, are different, the CATE wrt. representations is identifiable from observational data $\mathbb{P}(\Phi(X), A, Y)$ due to the exchangeability wrt. representations, $A \perp\!\!\!\perp (Y[0], Y[1]) \mid \Phi(X)$. This is seen in the following:

$$\tau^\phi(\phi) \stackrel{(ii)}{=} \mathbb{E}(Y[1] - Y[0] \mid \phi) = \mathbb{E}(Y[1] \mid A = 1, \phi) - \mathbb{E}(Y[0] \mid A = 0, \phi) = \mu_1^\phi(\phi) - \mu_0^\phi(\phi). \quad (8)$$

(ii) **Representation-induced confounding bias (RICB).** This situation happens when information about X^Δ is lost or when M-bias is introduced, i. e., some information is lost about both X^a and X^y but not $X^{\emptyset, m}$. Yet, M-bias is rather a theoretic concept and rarely appears in real-world studies (Ding & Miratrix, 2015); therefore, we further concentrate on the loss of confounder information in representations. As described previously, the information on X^Δ could be lost due to an incorrectly chosen dimensionality of the representation or due to too large balancing with an empirical probability metric. In this case, in addition to the loss of heterogeneity, we have *representation-induced confounding bias* (RICB). That is, the CATE wrt. representations is *non-identifiable* from observational data, $\mathbb{P}(\Phi(X), A, Y)$. This follows from

$$\tau^\phi(\phi) \stackrel{(ii)}{=} \mathbb{E}(Y[1] - Y[0] | \phi) \neq \mathbb{E}(Y[1] | A = 1, \phi) - \mathbb{E}(Y[0] | A = 0, \phi) = \mu_1^\phi(\phi) - \mu_0^\phi(\phi). \quad (9)$$

Technically, both the CATE wrt. representations, $\tau^\phi(\phi)$, and the RIBC, $\tau^\phi(\phi) - (\mu_1^\phi(\phi) - \mu_0^\phi(\phi))$, are still identifiable from $\mathbb{P}(X, A, Y)$. Yet, the identification formula has intractable integration in Eq. (8) and the original CATE wrt. covariates, which makes the whole inference senseless.

Motivated by this, we shift our focus in the following section to *partial identification* of the CATE wrt. to representations (or, equivalently, the RIBC), as partial identification turns out to be tractable. As a result, we can provide bounds for both quantities. With a slight abuse of formulations, we use ‘the bounds on the RIBC’ and ‘the bounds on the representation CATE’ interchangeably, as one can be inferred from the other.

Takeaways. (1) The minimal sufficient and valid representation would aim to remove only the information about noise and instruments (Ding et al., 2017; Johansson et al., 2022). In low-sample settings, we cannot guarantee that any information is preserved in a low-dimensional representation, so we a priori assume that some information is lost about the sub-covariates. (2) The loss of heterogeneity does not introduce bias but can only make CATE less individualized, namely, suitable only for subgroups. For many applications, like medicine and policy making, subgroup-level CATE is sufficient. (3) The RIBC automatically implies a loss of heterogeneity. Therefore, we consider the RIBC to be the main problem in representation learning methods for CATE, and, in this paper, we thus aim at providing bounds on the RIBC, as the exact value is intractable.

4 PARTIAL IDENTIFICATION OF CATE UNDER RICB

In the following, we use the marginal sensitivity model to derive bounds on the RIBC (Sec. 4.1). Then, we present a neural refutation framework for estimating the bounds, which can be used with any representation learning method for CATE (Sec. 4.2). Here, we do not assume the specific partitioning of X (which we did before in Sec. 3.1 only for the purpose of providing a better intuition).

4.1 BOUNDS ON THE RICB

We now aim to derive lower and upper bounds on the RIBC given by $\tau^\phi(\phi)$ and $\overline{\tau^\phi(\phi)}$, respectively.⁴ For this, we adopt the marginal sensitivity model (MSM) for CATE with binary treatment (Kallus et al., 2019; Jesson et al., 2021; Dorn & Guo, 2022; Oprescu et al., 2023; Frauen et al., 2023).

The MSM assumes that the odds ratio between the covariate (complete) propensity scores and the representation (nominal) propensity scores can be bounded. Applied to our setting, the MSM assumes

$$\Gamma(\phi)^{-1} \leq (\pi_0^\phi(\phi)/\pi_1^\phi(\phi)) (\pi_1^x(x)/\pi_0^x(x)) \leq \Gamma(\phi) \quad \text{for all } x \in \mathcal{X} \text{ s.t. } \Phi(x) = \phi, \quad (10)$$

where $\Gamma(\phi) \geq 1$ is a representation-dependent sensitivity parameter. In our setting, there are no undeserved confounders, and, therefore, the sensitivity parameters can be directly estimated from combined data $\mathbb{P}(X, \Phi(X), A, Y)$.⁵

We make the following observations. For $\Gamma(\phi) = 1$ for all ϕ , then (1) all the information about the propensity score $\pi_a^x(x)$ is preserved in the representation $\Phi(x)$, and (2) the representation does not contain hidden confounding. If $\Gamma(\phi) \gg 1$, we lose the treatment assignment information and

⁴The interval $[\tau^\phi(\phi), \overline{\tau^\phi(\phi)}]$ contains intractable $\tau^\phi(\phi)$ and can be inferred from $\mathbb{P}(\Phi(X), A, Y)$ and tractable sensitivity parameters.

⁵Note that this is a crucial *difference* from other applications of the MSM aimed at settings with unobserved confounding, where, instead, the sensitivity parameter is assumed chosen from background knowledge.

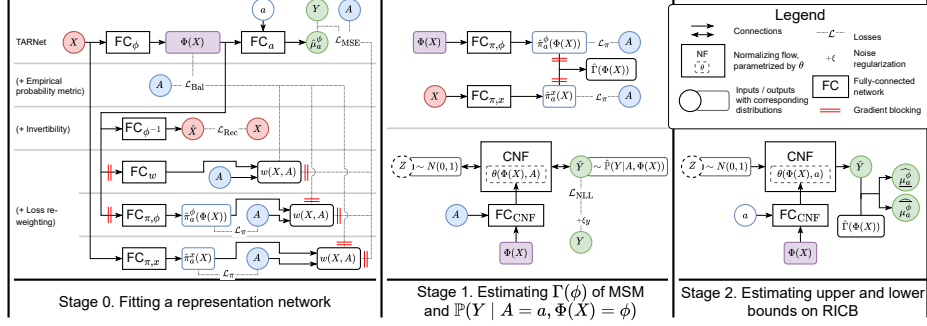


Figure 2: Our neural refutation framework for estimating bounds on the RICB. In **Stage 0**, we fit some representation learning method for CATE, possibly with different constraints like balancing with an empirical probability metric and invertibility, or loss re-weighting. In **Stage 1**, we estimate the sensitivity parameters of the MSM, $\Gamma(\phi)$, and the representation-conditional outcome distribution, $\mathbb{P}(Y | A = a, \Phi(X) = \phi)$. In **Stage 2**, we compute the lower and upper bounds on the RICB.

confounding bias could be introduced. Therefore, $\Gamma(\phi)$ indicates how much information is lost about sub-covariates X^a or about X^Δ . In order to actually distinguish whether we lose information specifically about X^a or X^Δ , we would need to know $\mu_a^x(x)$, which makes the task of representation learning for CATE obsolete. Thus, our bounds are conservative in the sense, that they grow if the information on X^a is lost, even though it does not lead to the RICB.

Under the assumption in Eq. (10), bounds (Frauen et al., 2023; Oprescu et al., 2023) on the RICB are given by

$$\underline{\tau}^\phi(\phi) = \underline{\mu}_1^\phi(\phi) - \overline{\mu}_0^\phi(\phi) \quad \text{and} \quad \overline{\tau}^\phi(\phi) = \overline{\mu}_1^\phi(\phi) - \underline{\mu}_0^\phi(\phi) \quad (11)$$

with

$$\begin{aligned} \underline{\mu}_a^\phi(\phi) &= \frac{1}{s_-(a, \phi)} \int_{-\infty}^{\mathbb{F}^{-1}(c_- | a, \phi)} y \mathbb{P}(Y = y | a, \phi) dy + \frac{1}{s_+(a, \phi)} \int_{\mathbb{F}^{-1}(c_- | a, \phi)}^{+\infty} y \mathbb{P}(Y = y | a, \phi) dy, \\ \overline{\mu}_a^\phi(\phi) &= \frac{1}{s_+(a, \phi)} \int_{-\infty}^{\mathbb{F}^{-1}(c_+ | a, \phi)} y \mathbb{P}(Y = y | a, \phi) dy + \frac{1}{s_-(a, \phi)} \int_{\mathbb{F}^{-1}(c_+ | a, \phi)}^{+\infty} y \mathbb{P}(Y = y | a, \phi) dy, \end{aligned}$$

where $s_-(a, \phi) = ((1 - \Gamma(\phi))\pi_a^\phi(\phi) + \Gamma(\phi))^{-1}$, $s_+(a, \phi) = ((1 - \Gamma(\phi)^{-1})\pi_a^\phi(\phi) + \Gamma(\phi)^{-1})^{-1}$, $c_- = 1/(1 + \Gamma(\phi))$, $c_+ = \Gamma(\phi)/(1 + \Gamma(\phi))$, $\mathbb{P}(Y = y | a, \phi) = \mathbb{P}(Y = y | A = a, \Phi(X) = \phi)$ is a representation-conditional density of the outcome, and $\mathbb{F}^{-1}(c | a, \phi)$ its corresponding quantile function. This result is an adaptation of the theoretic results, provided in (Frauen et al., 2023; Oprescu et al., 2023). We provide more details on the derivation of the bounds in Lemma 3 of Appendix B. Importantly, the bounds provided Eq. (11) are **valid** and **sharp** (see Corollary 1 in Appendix B). Validity means that our bounds always contain the ground-truth CATE wrt. representations, and sharpness means that the bounds only include CATE wrt. representations induced by the observational distributions complying with the sensitivity constraint from Eq. (10).

The above bounds are not easy to compute (which motivates our neural refutation framework in the following section). The reason is that the bounds on the RICB require inference of so-called conditional values at risk (CVaR) (Artzner et al., 1999; Kallus, 2023). Formally, we have two CVaRs given by $\int_{-\infty}^q \mathbb{P}(Y = y | a, \phi)$ and $\int_q^{+\infty} \mathbb{P}(Y = y | a, \phi)$ for $q \in \{\mathbb{F}^{-1}(c_- | a, \phi), \mathbb{F}^{-1}(c_+ | a, \phi)\}$. CVaRs can be estimated directly without estimating the conditional density, like in (Oprescu et al., 2023). Yet, in our case c_- and c_+ depend on ϕ , and, thus, it is more practical to estimate the conditional density, as done in (Frauen et al., 2023). Given some conditional density estimator, $\hat{\mathbb{P}}(Y = y | a, \phi)$, we can then estimate CVaRs via importance sampling, i. e.,

$$\widehat{\text{CVaR}} = \begin{cases} \frac{1}{k} \sum_{i=1}^{\lfloor kc \rfloor} \tilde{y}_i, & \text{for CVaR} = \int_{-\infty}^{\mathbb{F}^{-1}(c | a, \phi)} \mathbb{P}(Y = y | a, \phi), \\ \frac{1}{k} \sum_{i=\lfloor kc \rfloor + 1}^k \tilde{y}_i, & \text{for CVaR} = \int_{\mathbb{F}^{-1}(c | a, \phi)}^{+\infty} \mathbb{P}(Y = y | a, \phi), \end{cases} \quad (12)$$

where $\{\tilde{y}_i\}_{i=1}^k$ is a sorted sample from $\hat{\mathbb{P}}(Y | a, \phi)$. Hence, we use a conditional density estimator in our refutation framework.

4.2 NEURAL REFUTATION FRAMEWORK FOR ESTIMATING BOUNDS

In the following, we provide a flexible neural refutation framework for estimating the bounds on the RICB (see Fig. 2 for the overview). Overall, our refutation framework proceeds in three stages.

Table 2: Results for synthetic experiments. Reported: out-sample policy error rates (with improvements of our bounds); mean over 10 runs. Here, $n_{\text{train}} = 1,000$ and $\delta = 0.0005$.

d_ϕ	ER _{out} (Δ ER _{out})	
	1	2
TARNet	30.79% (-12.89%)	9.82% (-3.73%)
BNN (MMD; $\alpha = 0.1$)	34.32% (-15.41%)	16.15% (-4.19%)
CFR (MMD; $\alpha = 0.1$)	35.01% (-14.27%)	11.92% (-5.54%)
CFR (MMD; $\alpha = 0.5$)	35.79% (-11.43%)	17.89% (-7.27%)
CFR (WM; $\alpha = 1.0$)	34.97% (-14.27%)	10.88% (-7.97%)
CFR (WM; $\alpha = 2.0$)	35.18% (-13.63%)	13.19% (-6.28%)
InvTARNet	29.51% (-0.95%)	5.64% (-0.02%)
RCFR (WM; $\alpha = 1.0$)	33.02% (-3.58%)	8.00% (-4.27%)
CFR-ISW (WM; $\alpha = 1.0$)	35.00% (-9.43%)	7.27% (-1.86%)
BWCFR (WM; $\alpha = 1.0$)	34.97% (-10.02%)	7.44% (-4.57%)

Classical CATE estimators: k -NN: 8.18%; BART: 17.37%; C-Forest: 16.10%

Table 3: Results for HC-MNIST experiments. Reported: out-sample policy error rates (with improvements of our bounds); mean over 10 runs. Here, $\delta = 0.0005$.

d_ϕ	ER _{out} (Δ ER _{out})		
	7	39	78
TARNet	11.21% (-2.59%)	10.91% (-3.34%)	11.01% (-2.62%)
BNN (MMD; $\alpha = 0.1$)	12.00% (-4.50%)	11.37% (-5.29%)	20.78% (-2.01%)
CFR (MMD; $\alpha = 0.1$)	11.40% (-1.89%)	11.05% (-3.13%)	11.73% (-4.67%)
CFR (MMD; $\alpha = 0.5$)	16.01% (+19.25%)	12.55% (-4.95%)	12.90% (-5.25%)
CFR (WM; $\alpha = 1.0$)	24.55% (-10.42%)	27.87% (-10.18%)	31.19% (-11.53%)
CFR (WM; $\alpha = 2.0$)	31.71% (-10.34%)	30.77% (-7.22%)	31.83% (-11.91%)
InvTARNet	12.18% (-1.29%)	11.38% (-3.98%)	11.55% (-4.34%)
RCFR (WM; $\alpha = 1.0$)	21.51% (-9.17%)	26.97% (-6.17%)	30.14% (-14.26%)
CFR-ISW (WM; $\alpha = 1.0$)	32.64% (-10.32%)	26.66% (-11.30%)	30.02% (-13.31%)
BWCFR (WM; $\alpha = 1.0$)	13.62% (-3.96%)	28.18% (+0.24%)	32.54% (-6.75%)

Lower = better. Improvement over the baseline in green, worsening of the baseline in red
Classical CATE estimators: k -NN: 22.34%; BART: 17.51%; C-Forest: 17.65%

Stage 0. The initial stage is a naive application of existing representation learning methods for CATE estimation. As such, we fit a standard representation learning method for the CATE of our choice (e. g., TARNet, CFR, or different variants of CFR). Stage 0 always contains a fully-connected representation subnetwork, FC_ϕ , which takes covariates X as an input and outputs the representation, $\Phi(X)$. Similarly, potential outcomes predicting subnetwork(s) are also fully-connected, FC_a . Together, FC_ϕ and FC_a aim to minimize a (potentially weighted) mean squared error of the factual observational data, \mathcal{L}_{MSE} . The representation can be further constrained via (a) balancing with an empirical probability metric, (b) invertibility, or have additional (c) loss re-weighting. These are as follows. (a) Balancing, \mathcal{L}_{Bal} is implemented with either Wasserstein metric (WM) or maximum mean discrepancy (MMD) with loss coefficient α (Johansson et al., 2016; Shalit et al., 2017). (b) Invertibility (Zhang et al., 2020) is enforced with a reconstruction subnetwork, $\text{FC}_{\phi^{-1}}$, and a reconstruction loss, \mathcal{L}_{Rec} . (c) Loss re-weighting is done by employing either trainable weights (Johansson et al., 2018; 2022), with a fully-connected FC_w ; with a representation-propensity subnetwork (Hassanpour & Greiner, 2019a;b), $\text{FC}_{\pi,\phi}$; or with a covariate-propensity subnetwork (Assaad et al., 2021), namely $\text{FC}_{\pi,x}$.

Stage 1. Here, we use the trained representation subnetwork and then estimate the sensitivity parameters, $\Gamma(\phi)$, and representation-conditional outcome distribution, $\mathbb{P}(Y | A = a, \Phi(X) = \phi)$. For that, we train two fully-connected propensity networks, $\text{FC}_{\pi,\phi}$ and $\text{FC}_{\pi,x}$ (or take them from the Stage 0, if they were used for (c) loss re-weighting). Both networks optimize a binary cross-entropy (BCE) loss, \mathcal{L}_π . Then, we use Eq. (10) to compute $\hat{\Gamma}(\phi_i)$ for $\phi_i = \Phi(x_i)$ with x_i from \mathcal{D} . Specifically, each $\hat{\Gamma}(\phi_i)$ is a maximum over all $\hat{\Gamma}(\Phi(x_j))$, where $\Phi(x_j)$ are the representations of the training sample in δ -ball around ϕ_i . Here, δ is a hyperparameter, whose misspecification only makes the bounds more conservative but does not influence their validity. In addition, we estimate the representation-conditional outcome density with a conditional normalizing flow (CNF) (Trippe & Turner, 2018) using a fully-connected context subnetwork, FC_{CNF} . The latter aims at minimizing the negative log-likelihood of the observational data, \mathcal{L}_{NLL} .

Stage 2. Finally, we compute the lower and upper bounds on the RICB, as described in Eq.(11)–(12). Here, the CNF is beneficial for our task, as it enables direct sampling from the estimated conditional distribution. Further details on implementation details and hyperparameter tuning are in Appendix C.

5 EXPERIMENTS

Setup. We empirically validate our bounds on the RICB.⁶ For that, we use several (semi-)synthetic benchmarks with ground-truth counterfactual outcomes $Y[0]$ and $Y[1]$ and ground-truth CATE $\tau^x(x)$. Inspired by Jesson et al. (2021), we designed our experiments so that we compare policies based on (a) the estimated CATE or (b) the estimated bounds on the RICB. In (a), a policy based on the point estimate of the CATE applies a treatment whenever the CATE is positive, i.e. $\hat{\pi}(\phi) = \mathbb{1}\{\hat{\tau}^\phi(\phi) > 0\}$. In (b), a policy $\pi^*(\phi)$ based on the bounds on the RICB has three decisions: (1) to treat, i.e., when $\hat{\tau}^\phi(\phi) > 0$; (2) to do nothing, i.e., when $\hat{\tau}^\phi(\phi) < 0$; and (3) to defer a decision, otherwise.

⁶We also considered other evaluation techniques. However, the ground-truth CATE wrt. representations is intractable; therefore, one can *not* employ established metrics such as coverage or compare MSEs directly. As a remedy, we follow Jesson et al. (2021) and evaluate the decision-making under our CATE, which is closely aligned with how our refutation framework would be used for making reliable decisions in practice.

Table 4: Results for IHDP100 experiments. Reported: out-sample policy error rates (with improvements of our bounds); mean over 100 train/test splits. Here, $\delta = 0.0005$.

d_ϕ	ER _{out} (Δ ER _{out})				
	5	10	15	20	25
TARNet	3.17% (-2.65%)	2.88% (-2.30%)	3.28% (-2.74%)	3.23% (-2.52%)	2.89% (-2.37%)
BNN (MMD; $\alpha = 0.1$)	2.32% (-1.49%)	2.43% (-1.40%)	2.59% (-2.03%)	2.43% (-1.87%)	2.29% (-1.16%)
CFR (MMD; $\alpha = 0.1$)	1.77% (-0.89%)	2.09% (-1.03%)	2.23% (-1.63%)	1.88% (-0.48%)	2.04% (-1.46%)
CFR (MMD; $\alpha = 0.5$)	2.07% (-1.46%)	2.00% (+3.98%)	2.68% (+1.89%)	2.36% (+6.37%)	2.17% (+3.41%)
CFR (WM; $\alpha = 1.0$)	1.93% (-0.89%)	1.75% (-0.25%)	1.83% (-1.24%)	1.83% (-0.49%)	1.80% (-0.20%)
CFR (WM; $\alpha = 2.0$)	1.97% (-0.04%)	2.17% (-1.49%)	2.05% (-1.21%)	2.08% (-1.29%)	2.09% (-1.36%)
InvTARNet	2.52% (-1.95%)	3.11% (-2.47%)	2.99% (-2.51%)	2.79% (-2.41%)	2.83% (-2.28%)
RCFR (WM; $\alpha = 1.0$)	3.36% (-2.84%)	3.45% (-1.52%)	2.67% (-1.57%)	4.69% (-3.83%)	1.95% (+1.06%)
CFR-ISW (WM; $\alpha = 1.0$)	2.24% (-0.96%)	1.93% (-0.68%)	1.71% (-1.18%)	1.85% (-1.54%)	1.88% (-0.19%)
BWCFR (WM; $\alpha = 1.0$)	3.57% (-1.49%)	3.52% (-2.16%)	3.88% (-1.10%)	3.80% (-2.38%)	4.07% (-1.18%)

Lower = better. Improvement over the baseline in green, worsening of the baseline in red
 Classical CATE estimators: k -NN: 7.47%; BART: 5.07%; C-Forest: 6.28%

Evaluation metric. To compare our bounds with the point estimates, we employ an error rate of the policy (ER). ER is defined as the rate of how often decisions of the estimated policy are different from the decision of the optimal policy, $\pi(x) = \mathbb{1}\{\tau^x(x) > 0\}$. For the policy based on our bounds, we report the error rate on the non-deferred decisions. Hence, improvements over the baselines due to our refutation framework would imply that our bounds are precise and that we defer the right observations/individuals. Additionally, we report a root precision in estimating treatment effect (rPEHE) of original methods in Appendix E.

Baselines. We combine our refutation framework with the state-of-the-art baselines from representation learning. These are: **TARNet** (Shalit et al., 2017; Johansson et al., 2022) implements a representation network without constraints; **BNN** (Johansson et al., 2016) enforces balancing with MMD ($\alpha = 0.1$); **CFR** (Shalit et al., 2017; Johansson et al., 2022) is used in four variants of balancing with WM ($\alpha = 1.0/2.0$) and with MMD ($\alpha = 0.1/0.5$). **InvTARNet** adds an invertibility constraint to the TARNet via the reconstruction loss, as in (Zhang et al., 2020). Finally, three methods use additional loss re-weighting on top of the balancing with WM ($\alpha = 1.0$): **RCFR** (Johansson et al., 2018; 2022), **CFR-ISW** (Hassanpour & Greiner, 2019a), and **BWCFR** (Assaad et al., 2021). Also, for reference, we provide results for classical (non-neural) CATE estimators, i. e., k -NN regression, Bayesian additive regression trees (**BART**) (Chipman et al., 2010), and causal forests (**C-Forest**) (Wager & Athey, 2018).

■ **Synthetic data.** We adapt the synthetic data generator from Kallus et al. (2019), where we add an unobserved confounder to the observed covariates so that $d_x = 2$. We sample $n_{\text{train}} \in \{500; 1,000; 5,000; 10,000\}$ training and $n_{\text{test}} = 1,000$ datapoints. Further details are in Appendix D. We plot ground-truth and estimated decision boundaries in Appendix E. Additionally, in Table 2, we provide error rates of the original representation learning methods and improvements in error rates with our bounds. Our refutation framework achieves clear improvements in the error rate among all the baselines. This improvement is especially large, when $d_\phi = 1$, so that there are both the loss of heterogeneity and the RICB.

■ **IHDP100 dataset.** The Infant Health and Development Program (IHDP) (Hill, 2011; Shalit et al., 2017) is a classical benchmark for CATE estimation and consists of the 100 train/test splits with $n_{\text{train}} = 672, n_{\text{test}} = 75, d_x = 25$. Again, our refutation framework improves the error rates for almost all of the baselines (Table 4). We observe one deviation for CFR (MMD; $\alpha = 0.5$), but this can be explained by too large balancing with an empirical probability metric and the low-sample size.

■ **HC-MNIST dataset.** HC-MNIST is a semi-synthetic benchmark on top of the MNIST image dataset (Jesson et al., 2021). We consider all covariates as observed (see Appendix D). The challenge in CATE estimation comes from the high-dimensionality of covariates, i. e., $d_x = 784 + 1$. Again, our refutation framework improves over the baselines by a clear margin (see Table 3).

Additional results. In Appendix E, we provide additional results, where we report deferral rates in addition to the error rates for different values of the hyperparameter δ . Our refutation framework reduces the error rates while increasing the deferral rates not too much, which demonstrates its effectiveness.

Conclusion. We studied the validity of representation learning for CATE estimation. The validity may be violated due to low-dimensional representations as these introduce a *representation-induced confounding bias*. As a remedy, we introduced a novel, representation-agnostic refutation framework that practitioners can use to estimate bounds on the RICB and thus improve the reliability of their CATE estimator.

Acknowledgments. S.F. acknowledges funding via Swiss National Science Foundation Grant 186932.

REFERENCES

- Ahmed M. Alaa and Mihaela van der Schaar. Bayesian inference of individualized treatment effects using multi-task Gaussian processes. In *Advances in Neural Information Processing Systems*, 2017.
- Ahmed M. Alaa and Mihaela van der Schaar. Bayesian nonparametric causal inference: Information rates and learning algorithms. *IEEE Journal of Selected Topics in Signal Processing*, 12:1031–1046, 2018a.
- Ahmed M. Alaa and Mihaela van der Schaar. Limits of estimating heterogeneous treatment effects: Guidelines for practical algorithm design. In *International Conference on Machine Learning*, 2018b.
- Tara V. Anand, Adele H. Ribeiro, Jin Tian, and Elias Bareinboim. Causal effect identification in cluster DAGs. In *AAAI Conference on Artificial Intelligence*, 2023.
- Philippe Artzner, Freddy Delbaen, Jean-Marc Eber, and David Heath. Coherent measures of risk. *Mathematical Finance*, 9(3):203–228, 1999.
- Serge Assaad, Shuxi Zeng, Chenyang Tao, Shounak Datta, Nikhil Mehta, Ricardo Henao, Fan Li, and Lawrence Carin. Counterfactual representation learning with balancing weights. In *International Conference on Artificial Intelligence and Statistics*, 2021.
- Onur Atan, William R. Zame, and Mihaela van der Schaar. Counterfactual policy optimization using domain-adversarial neural networks. 2018.
- Ioana Bica, Ahmed M. Alaa, James Jordon, and Mihaela van der Schaar. Estimating counterfactual treatment outcomes over time through adversarially balanced representations. In *International Conference on Learning Representations*, 2020.
- Matthew Blackwell. A selection bias approach to sensitivity analysis for causal effects. *Political Analysis*, 22(2):169–182, 2014.
- Matteo Bonvini, Edward Kennedy, Valerie Ventura, and Larry Wasserman. Sensitivity analysis for marginal structural models. *arXiv preprint arXiv:2210.04681*, 2022.
- Victor Chernozhukov, Denis Chetverikov, Mert Demirer, Esther Duflo, Christian Hansen, and Whitney Newey. Double/debiased/Neyman machine learning of treatment effects. *American Economic Review*, 107(5):261–265, 2017.
- Hugh A. Chipman, Edward I. George, and Robert E. McCulloch. BART: Bayesian additive regression trees. *The Annals of Applied Statistics*, 4(1), 2010.
- Carlos Cinelli, Andrew Forney, and Judea Pearl. A crash course in good and bad controls. *Sociological Methods & Research*, 2022.
- Amanda Coston, Edward Kennedy, and Alexandra Chouldechova. Counterfactual predictions under runtime confounding. *Advances in Neural Information Processing Systems*, 2020.
- Alicia Curth and Mihaela van der Schaar. On inductive biases for heterogeneous treatment effect estimation. *Advances in Neural Information Processing Systems*, 2021a.
- Alicia Curth and Mihaela van der Schaar. Nonparametric estimation of heterogeneous treatment effects: From theory to learning algorithms. In *International Conference on Artificial Intelligence and Statistics*, 2021b.
- Peng Ding and Luke W. Miratrix. To adjust or not to adjust? Sensitivity analysis of M-bias and butterfly-bias. *Journal of Causal Inference*, 3(1):41–57, 2015.

- Peng Ding, T.J. VanderWeele, and James M. Robins. Instrumental variables as bias amplifiers with general outcome and confounding. *Biometrika*, 104(2):291–302, 2017.
- Jacob Dorn and Kevin Guo. Sharp sensitivity analysis for inverse propensity weighting via quantile balancing. *Journal of the American Statistical Association*, pp. 1–13, 2022.
- Xin Du, Lei Sun, Wouter Duivesteijn, Alexander Nikolaev, and Mykola Pechenizkiy. Adversarial balancing-based representation learning for causal effect inference with observational data. *Data Mining and Knowledge Discovery*, 35(4):1713–1738, 2021.
- Conor Durkan, Artur Bekasov, Iain Murray, and George Papamakarios. Neural spline flows. In *Advances in Neural Information Processing Systems*, 2019.
- Stefan Feuerriegel, Dennis Frauen, Valentyn Melnychuk, Jonas Schweisthal, Konstantin Hess, Alicia Curth, Stefan Bauer, Niki Kilbertus, Isaac S. Kohane, and Mihaela van der Schaar. Causal machine learning for predicting treatment outcomes. *Nature Medicine*, 2024.
- Dennis Frauen, Valentyn Melnychuk, and Stefan Feuerriegel. Sharp bounds for generalized causal sensitivity analysis. In *Advances in Neural Information Processing Systems*, 2023.
- Xingzhuo Guo, Yuchen Zhang, Jianmin Wang, and Mingsheng Long. Estimating heterogeneous treatment effects: Mutual information bounds and learning algorithms. In *International Conference on Machine Learning*, 2023.
- Ben B. Hansen. The prognostic analogue of the propensity score. *Biometrika*, 95(2):481–488, 2008.
- Negar Hassanpour and Russell Greiner. Counterfactual regression with importance sampling weights. In *International Joint Conference on Artificial Intelligence*, 2019a.
- Negar Hassanpour and Russell Greiner. Learning disentangled representations for counterfactual regression. In *International Conference on Learning Representations*, 2019b.
- Konstantin Hess, Valentyn Melnychuk, Dennis Frauen, and Stefan Feuerriegel. Bayesian neural controlled differential equations for treatment effect estimation. In *International Conference on Learning Representations*, 2024.
- Jennifer L. Hill. Bayesian nonparametric modeling for causal inference. *Journal of Computational and Graphical Statistics*, 20(1):217–240, 2011.
- Zonghui Hu, Dean A. Follmann, and Naisyin Wang. Estimation of mean response via the effective balancing score. *Biometrika*, 101(3):613–624, 2014.
- Ming-Yueh Huang and Kwun Chuen Gary Chan. Joint sufficient dimension reduction and estimation of conditional and average treatment effects. *Biometrika*, 104(3):583–596, 2017.
- Guido Imbens and Joshua Angrist. Identification and estimation of local average treatment effects. *Econometrica*, 62(2):467–475, 1994.
- Andrew Jesson, Sören Mindermann, Uri Shalit, and Yarin Gal. Identifying causal-effect inference failure with uncertainty-aware models. In *Advances in Neural Information Processing Systems*, 2020.
- Andrew Jesson, Sören Mindermann, Yarin Gal, and Uri Shalit. Quantifying ignorance in individual-level causal-effect estimates under hidden confounding. In *International Conference on Machine Learning*, 2021.
- Fredrik D. Johansson, Uri Shalit, and David Sontag. Learning representations for counterfactual inference. In *International Conference on Machine Learning*, 2016.
- Fredrik D. Johansson, Nathan Kallus, Uri Shalit, and David Sontag. Learning weighted representations for generalization across designs. *arXiv preprint arXiv:1802.08598*, 2018.
- Fredrik D. Johansson, Uri Shalit, Nathan Kallus, and David Sontag. Generalization bounds and representation learning for estimation of potential outcomes and causal effects. *Journal of Machine Learning Research*, 23:7489–7538, 2022.

- Nathan Kallus. Treatment effect risk: Bounds and inference. *Management Science*, 69(8):4579–4590, 2023.
- Nathan Kallus, Xiaojie Mao, and Angela Zhou. Interval estimation of individual-level causal effects under unobserved confounding. In *International Conference on Artificial Intelligence and Statistics*, 2019.
- Edward H. Kennedy. Towards optimal doubly robust estimation of heterogeneous causal effects. *Electronic Journal of Statistics*, 17(2):3008–3049, 2023.
- Edward H. Kennedy, Sivaraman Balakrishnan, James M. Robins, and Larry Wasserman. Minimax rates for heterogeneous causal effect estimation. *arXiv preprint arXiv:2203.00837*, 2022.
- Mathias Kraus, Stefan Feuerriegel, and Maytal Saar-Tsechansky. Data-driven allocation of preventive care with application to diabetes mellitus type II. *Manufacturing & Service Operations Management*, 2023.
- Sören R. Künzel, Jasjeet S. Sekhon, Peter J. Bickel, and Bin Yu. Metalearners for estimating heterogeneous treatment effects using machine learning. *Proceedings of the National Academy of Sciences*, 116(10):4156–4165, 2019.
- Yann LeCun. The MNIST database of handwritten digits. <http://yann.lecun.com/exdb/mnist/>, 1998.
- Ilya Loshchilov and Frank Hutter. Decoupled weight decay regularization. In *International Conference on Learning Representations*, 2019.
- Valentyn Melnychuk, Dennis Frauen, and Stefan Feuerriegel. Causal transformer for estimating counterfactual outcomes. In *International Conference on Machine Learning*, 2022.
- Xinkun Nie and Stefan Wager. Quasi-oracle estimation of heterogeneous treatment effects. *Biometrika*, 108:299–319, 2021.
- Miruna Oprescu, Jacob Dorn, Marah Ghoummaid, Andrew Jesson, Nathan Kallus, and Uri Shalit. B-learner: Quasi-oracle bounds on heterogeneous causal effects under hidden confounding. In *International Conference on Machine Learning*, 2023.
- James M. Robins, Andrea Rotnitzky, and Daniel O. Scharfstein. Sensitivity analysis for selection bias and unmeasured confounding in missing data and causal inference models. *IMA Volumes in Mathematics and its Applications*, 116:1–94, 2000.
- Jonas Rothfuss, Fabio Ferreira, Simon Boehm, Simon Walther, Maxim Ulrich, Tamim Asfour, and Andreas Krause. Noise regularization for conditional density estimation. *arXiv preprint arXiv:1907.08982*, 2019.
- P. K. Rubenstein, S. Weichwald, S. Bongers, J. M. Mooij, D. Janzing, M. Grosse-Wentrup, and B. Schölkopf. Causal consistency of structural equation models. In *Conference on Uncertainty in Artificial Intelligence*, 2017.
- Donald B. Rubin. Estimating causal effects of treatments in randomized and nonrandomized studies. *Journal of Educational Psychology*, 66(5):688, 1974.
- Patrick Schwab, Lorenz Linhardt, and Walter Karlen. Perfect match: A simple method for learning representations for counterfactual inference with neural networks. *arXiv preprint arXiv:1810.00656*, 2018.
- Nabeel Seedat, Fergus Imrie, Alexis Bellot, Zhaozhi Qian, and Mihaela van der Schaar. Continuous-time modeling of counterfactual outcomes using neural controlled differential equations. In *International Conference on Machine Learning*, 2022.
- Uri Shalit, Fredrik D. Johansson, and David Sontag. Estimating individual treatment effect: Generalization bounds and algorithms. In *International Conference on Machine Learning*, 2017.
- Zhiqiang Tan. A distributional approach for causal inference using propensity scores. *Journal of the American Statistical Association*, 101(476):1619–1637, 2006.

- Brian L. Trippe and Richard E. Turner. Conditional density estimation with Bayesian normalising flows. *arXiv preprint arXiv:1802.04908*, 2018.
- Hal R. Varian. Causal inference in economics and marketing. *Proceedings of the National Academy of Sciences*, 113(27):7310–7315, 2016.
- Stefan Wager and Susan Athey. Estimation and inference of heterogeneous treatment effects using random forests. *Journal of the American Statistical Association*, 113(523):1228–1242, 2018.
- Hao Wang, Jiajun Fan, Zhichao Chen, Haoxuan Li, Weiming Liu, Tianqiao Liu, Quanyu Dai, Yichao Wang, Zhenhua Dong, and Ruiming Tang. Optimal transport for treatment effect estimation. *Advances in Neural Information Processing Systems*, 2024.
- Anpeng Wu, Junkun Yuan, Kun Kuang, Bo Li, Runze Wu, Qiang Zhu, Yueting Zhuang, and Fei Wu. Learning decomposed representations for treatment effect estimation. *IEEE Transactions on Knowledge and Data Engineering*, 35(5):4989–5001, 2022.
- Anpeng Wu, Kun Kuang, Ruoxuan Xiong, Bo Li, and Fei Wu. Stable estimation of heterogeneous treatment effects. In *International Conference on Machine Learning*, 2023.
- Liuyi Yao, Sheng Li, Yaliang Li, Mengdi Huai, Jing Gao, and Aidong Zhang. Representation learning for treatment effect estimation from observational data. *Advances in Neural Information Processing Systems*, 2018.
- Yao Zhang, Alexis Bellot, and Mihaela van der Schaar. Learning overlapping representations for the estimation of individualized treatment effects. In *International Conference on Artificial Intelligence and Statistics*, 2020.

A EXTENDED RELATED WORK

CATE estimation. A wide range of machine learning methods have been employed for estimating CATE. Examples include tailored methods built on top of linear regression Johansson et al. (2016), regression trees (Chipman et al., 2010; Hill, 2011), and random forests (Wager & Athey, 2018). Alaa & van der Schaar (2017) proposed non-parametric approaches based on Gaussian processes. Later, it was shown in (Alaa & van der Schaar, 2018a;b), that Gaussian processes can achieve optimal minimax rates for non-parametric estimation, but only in asymptotic regime and under smoothness conditions.⁷ Another stream of literature studied meta-learners (Künzel et al., 2019; Kennedy, 2023; Nie & Wager, 2021; Kennedy et al., 2022), which combine different nuisance function estimators; and double/debiased machine learning (Chernozhukov et al., 2017), which turns CATE estimation into two-stage regression. Both approaches can achieve optimal convergence rates of CATE estimation, but, again, only asymptotically and with well-specified models. Curth & van der Schaar (2021a) and Curth & van der Schaar (2021b) specifically studied neural networks as base model classes for meta-learners. According to (Curth & van der Schaar, 2021b), representation learning methods are one-step (plug-in) learners and they aim at best-in-class estimation of CATE, given potentially misspecified parametric model classes (Johansson et al., 2022).

Prognostic scores. Inferring prognostic scores (Hansen, 2008) is relevant to CATE estimation with representation learning. The prognostic score is such a transformation of covariates, which preserves all the information about a potential outcome and can be seen as a sufficient dimensionality reduction technique for CATE. For example, linear prognostic scores were rigorously studied in (Hu et al., 2014; Huang & Chan, 2017). As mentioned by (Johansson et al., 2022), representation learning CATE estimators aim to learn approximate non-linear prognostic scores.

Uncertainty of CATE estimation. Several works studied uncertainty around CATE estimation. For example, Jesson et al. (2020) studied epistemic uncertainty, and Jesson et al. (2021) additionally considered bias due to unobserved confounding, which was a part of aleatoric uncertainty. Our work differs from both of them, as we aim at estimating the confounding bias, present in low-dimensional (potentially constrained) representations. This bias still persists in an infinite-sample regime, where epistemic uncertainty drops to zero.

Runtime confounding. Runtime confounding (Coston et al., 2020) arises when a subset of covariates is not available during prediction time. This setting is highly relevant, e. g., for multi-step-ahead prediction of time-varying methods where future time-varying covariates are not observed; and (questionably) some methods used balanced representations as a heuristic to circumvent this bias (Bica et al., 2020; Melnychuk et al., 2022; Seedat et al., 2022; Hess et al., 2024). Notably, non-availability of covariates can be seen as a special case of low-dimensional representations which zero-out some inputs and have identity transformations for the others. Therefore, runtime confounding is a special case of our proposed RICB.

⁷One important result of (Alaa & van der Schaar, 2018b) is that minimax rate of non-parametric estimation of CATE does not asymptotically depend on *treatment imbalance*. In a low-sample regime nevertheless, addressing treatment imbalance is still important.

Lemma 3 (MSM bounds on the RICB). *Let a representation $\phi = \Phi(x)$ satisfy the following sensitivity constraint:*

$$\Gamma(\phi)^{-1} \leq (\pi_0^\phi(\phi)/\pi_1^\phi(\phi)) (\pi_1^x(x)/\pi_0^x(x)) \leq \Gamma(\phi) \quad \text{for all } x \in \mathcal{X} \text{ s.t. } \Phi(x) = \phi, \quad (21)$$

where $\Gamma(\phi) \geq 1$ is a representation-dependent sensitivity parameter.

Under the assumption in Eq. (21), bounds (Frauen et al., 2023; Oprescu et al., 2023) on the RICB are given by

$$\underline{\tau}^\phi(\phi) = \underline{\mu}_1^\phi(\phi) - \overline{\mu}_0^\phi(\phi) \quad \text{and} \quad \overline{\tau}^\phi(\phi) = \overline{\mu}_1^\phi(\phi) - \underline{\mu}_0^\phi(\phi) \quad (22)$$

with

$$\begin{aligned} \underline{\mu}_a^\phi(\phi) &= \frac{1}{s_-(a, \phi)} \int_{-\infty}^{\mathbb{F}^{-1}(c_- | a, \phi)} y \mathbb{P}(Y = y | a, \phi) dy + \frac{1}{s_+(a, \phi)} \int_{\mathbb{F}^{-1}(c_- | a, \phi)}^{+\infty} y \mathbb{P}(Y = y | a, \phi) dy, \\ \overline{\mu}_a^\phi(\phi) &= \frac{1}{s_+(a, \phi)} \int_{-\infty}^{\mathbb{F}^{-1}(c_+ | a, \phi)} y \mathbb{P}(Y = y | a, \phi) dy + \frac{1}{s_-(a, \phi)} \int_{\mathbb{F}^{-1}(c_+ | a, \phi)}^{+\infty} y \mathbb{P}(Y = y | a, \phi) dy, \end{aligned}$$

where $s_-(a, \phi) = ((1 - \Gamma(\phi))\pi_a^\phi(\phi) + \Gamma(\phi))^{-1}$, $s_+(a, \phi) = ((1 - \Gamma(\phi)^{-1})\pi_a^\phi(\phi) + \Gamma(\phi)^{-1})^{-1}$, $c_- = 1/(1 + \Gamma(\phi))$, $c_+ = \Gamma(\phi)/(1 + \Gamma(\phi))$, $\mathbb{P}(Y = y | a, \phi) = \mathbb{P}(Y = y | A = a, \Phi(X) = \phi)$ is a representation-conditional density of the outcome, and $\mathbb{F}^{-1}(c | a, \phi)$ its corresponding quantile function.

Proof. We employ the main results from (Frauen et al., 2023).

First, it is easy to see, that our definition of the MSM, i. e., Eq. (21), fits to the definition of the generalized marginal sensitivity model (GMSM) from (Frauen et al., 2023). Specifically, we can rearrange the terms in Eq. (21) in the following way (see Appendix C.1 in (Frauen et al., 2023)):

$$\frac{1}{(1 - \Gamma)\pi_a^\phi(\phi) + \Gamma} \leq \frac{\pi_a^x(x)}{\pi_a^\phi(\phi)} \leq \frac{1}{(1 - \Gamma^{-1})\pi_a^\phi(\phi) + \Gamma^{-1}} \quad \text{for all } x \in \mathcal{X} \text{ s.t. } \Phi(x) = \phi, \quad (23)$$

where $a \in \{0, 1\}$. Then, we apply the Bayes rule to the inner ratio

$$\frac{\pi_a^x(x)}{\pi_a^\phi(\phi)} = \frac{\mathbb{P}(A = a | X = x, \Phi(X) = \Phi(x))}{\mathbb{P}(A = a | \Phi(X) = \Phi(x))} \quad (24)$$

$$= \frac{\mathbb{P}(X = x | \Phi(X) = \Phi(x), A = a) \pi_a^\phi(\phi)}{\mathbb{P}(X = x | \Phi(X) = \Phi(x)) \pi_a^\phi(\phi)} \quad (25)$$

$$= \frac{\mathbb{P}(X = x | \Phi(X) = \Phi(x), A = a)}{\mathbb{P}(X = x | \Phi(X) = \Phi(x), do(A = a))}, \quad (26)$$

where the latest equality holds, as the intervention on A , $do(A = a)$, does not change the conditional distribution of $\mathbb{P}(X | \Phi(X) = \Phi(x))$. Therefore, our definition of the MSM matches the definitions of the GMSM in (Frauen et al., 2023).

Second, to derive the bound on the RICB, we refer to Theorem 1 in (Frauen et al., 2023), which states that the lower and upper bounds are expectations of maximally left- and right-shifted interventional distributions, respectively. The maximally left-shifted distribution, $\mathbb{P}_-(Y | a, \phi)$, and the maximally right-shifted distribution, $\mathbb{P}_+(Y | a, \phi)$, are defined in the following way:

$$\mathbb{P}_-(Y = y | a, \phi) = \begin{cases} (1/s_-(a, \phi)) \mathbb{P}(Y = y | a, \phi), & \text{if } \mathbb{F}(y | a, \phi) \leq c_-, \\ (1/s_+(a, \phi)) \mathbb{P}(Y = y | a, \phi), & \text{if } \mathbb{F}(y | a, \phi) > c_-, \end{cases} \quad (27)$$

$$\mathbb{P}_+(Y = y | a, \phi) = \begin{cases} (1/s_+(a, \phi)) \mathbb{P}(Y = y | a, \phi), & \text{if } \mathbb{F}(y | a, \phi) \leq c_+, \\ (1/s_-(a, \phi)) \mathbb{P}(Y = y | a, \phi), & \text{if } \mathbb{F}(y | a, \phi) > c_+, \end{cases} \quad (28)$$

where $s_-(a, \phi) = ((1 - \Gamma(\phi))\pi_a^\phi(\phi) + \Gamma(\phi))^{-1}$, $s_+(a, \phi) = ((1 - \Gamma(\phi)^{-1})\pi_a^\phi(\phi) + \Gamma(\phi)^{-1})^{-1}$, $c_- = 1/(1 + \Gamma(\phi))$, $c_+ = \Gamma(\phi)/(1 + \Gamma(\phi))$, $\mathbb{P}(Y = y | a, \phi) = \mathbb{P}(Y = y | A = a, \Phi(X) = \phi)$ is a representation-conditional density of the outcome, and $\mathbb{F}(y | a, \phi)$ its corresponding CDF. Then, the lower and upper bounds can be obtained by taking expectations, i. e.,

$$\underline{\mu}_a^\phi(\phi) = \int_{\mathcal{Y}} y \mathbb{P}_-(Y = y | a, \phi) dy \quad \text{and} \quad \overline{\mu}_a^\phi(\phi) = \int_{\mathcal{Y}} y \mathbb{P}_+(Y = y | a, \phi) dy. \quad (29)$$

□

Corollary 1 (Validity and sharpness of bounds). *The bounds on the RICB in Lemma 3 are valid and sharp. Validity implies that the bounds always contain the ground-truth CATE wrt. representations, i. e., $\tau^\phi(\phi) \in [\underline{\tau}^\phi(\phi), \overline{\tau}^\phi(\phi)]$. Sharpness implies that all the values in the ignorance interval $[\underline{\tau}^\phi(\phi), \overline{\tau}^\phi(\phi)]$ are induced by the distributions which comply with the sensitivity constraint from Eq. (10).*

Proof. We refer to (Frauen et al., 2023) for a formal proof of both properties. □

C IMPLEMENTATION AND HYPERPARAMETERS

Implementation. We implemented our refutation framework in PyTorch and Pyro. For better compatibility, the fully-connected subnetworks have one hidden layer with a tuneable number of units. For the CNF, we employed neural spline flows (Durkan et al., 2019) with a standard normal as a base distribution and noise regularization (Rothfuss et al., 2019). The number of knots and the intensities of the noise regularization are hyperparameters. The CNF is trained via stochastic gradient descent (SGD) and all the other networks with AdamW (Loshchilov & Hutter, 2019). Each network was trained with $n_{iter} = 5,000$ train iterations.

Hyperparameters. We performed hyperparameter tuning at all the stages of our refutation framework for all the networks based on five-fold cross-validation using the training subset. At each stage, we did a random grid search with respect to different tuning criteria. Table 5 provides all the details on hyperparameters tuning. For reproducibility, we made tuned hyperparameters available in our GitHub.⁸

Table 5: Hyperparameter tuning for baselines and our refutation framework.

Stage	Model	Hyperparameter	Range / Value		
Stage 0	TARNet BNN CFR InvTARNet BWCFR	Learning rate	0.001, 0.005, 0.01		
		Minibatch size	32, 64, 128		
		Weight decay	0.0, 0.001, 0.01, 0.1		
		Hidden units in FC_ϕ ($FC_{\phi-1}$)	$Rd_x, 1.5 Rd_x, 2 Rd_x$		
		Hidden units in FC_a	$Rd_\phi, 1.5 Rd_\phi, 2 Rd_\phi$		
		Tuning strategy	random grid search with 50 runs		
		Tuning criterion	factual MSE loss		
		Optimizer	AdamW		
		Stage 0	CFR-ISW	Representation network learning rate	0.001, 0.005, 0.01
Propensity network learning rate	0.001, 0.005, 0.01				
Minibatch size	32, 64, 128				
Representation network weight decay	0.0, 0.001, 0.01, 0.1				
Propensity network weight decay	0.0, 0.001, 0.01, 0.1				
Hidden units in FC_ϕ	$Rd_x, 1.5 Rd_x, 2 Rd_x$				
Hidden units in FC_a	$Rd_\phi, 1.5 Rd_\phi, 2 Rd_\phi$				
Hidden units in $FC_{\pi,\phi}$	$Rd_\phi, 1.5 Rd_\phi, 2 Rd_\phi$				
Tuning strategy	random grid search with 100 runs				
Tuning criterion	factual MSE loss + factual BCE loss				
Optimizer	AdamW				
Stage 0	RCFR	Learning rate	0.001, 0.005, 0.01		
		Minibatch size	32, 64, 128		
		Weight decay	0.0, 0.001, 0.01, 0.1		
		Hidden units in FC_ϕ	$Rd_x, 1.5 Rd_x, 2 Rd_x$		
		Hidden units in FC_a	$Rd_\phi, 1.5 Rd_\phi, 2 Rd_\phi$		
		Hidden units in FC_w	$Rd_\phi, 1.5 Rd_\phi, 2 Rd_\phi$		
		Tuning strategy	random grid search with 50 runs		
		Tuning criterion	factual MSE loss		
		Optimizer	AdamW		
Stage 1	Propensity networks	Learning rate	0.001, 0.005, 0.01		
		Minibatch size	32, 64, 128		
		Weight decay	0.0, 0.001, 0.01, 0.1		
		Hidden units in $FC_{\pi,\phi x}$	$Rd_{\phi x}, 1.5 Rd_{\phi x}, 2 Rd_{\phi x}$		
		Tuning strategy	random grid search with 50 runs		
		Tuning criterion	factual BCE loss		
		Optimizer	AdamW		
		Stage 1	CNF	Learning rate	0.001, 0.005, 0.01
				Minibatch size	32, 64, 128
Hidden units in FC_{CNF}	$Rd_\phi, 1.5 Rd_\phi, 2 Rd_\phi$				
Number of knots	5, 10, 20				
Intensity of outcome noise	0.05, 0.1, 0.5				
Intensity of representation noise	0.05, 0.1, 0.5				
Tuning strategy	random grid search with 100 runs				
Tuning criterion	factual negative log-likelihood loss				
Optimizer	SGD (momentum = 0.9)				

$R = 2$ (synthetic data), $R = 1$ (IHDP100, HC-MNIST datasets)

⁸<https://github.com/Valentyn1997/RICB>.

D DATASET DETAILS

D.1 SYNTHETIC DATA

We adopt a synthetic benchmark with hidden confounding from (Kallus et al., 2019), but we add the confounder as the second observed covariate. Specifically, synthetic covariates, X_1 , X_2 , a treatment, A , and an outcome, Y , are sampled from the following data generating mechanism:

$$\begin{cases} X_1 \sim \text{Unif}(-2, 2), \\ X_2 \sim N(0, 1), \\ A \sim \text{Bern}\left(\frac{1}{1+\exp(-(0.75 X_1 - X_2 + 0.5))}\right) \\ Y \sim N((2A - 1)X_1 + A - 2 \sin(2(2A - 1)X_1 + X_2) - 2X_2(1 + 0.5X_1), 1), \end{cases} \quad (30)$$

where X_1, X_2 are mutually independent.

D.2 HC-MNIST DATASET

Jesson et al. (2021) introduced a complex high-dimensional, semi-synthetic dataset based on the MNIST image dataset (LeCun, 1998), namely HC-MNIST. The MNIST dataset contains $n_{\text{train}} = 60,000$ train and $n_{\text{test}} = 10,000$ test images. HC-MNIST takes original high-dimensional images and maps them onto a one-dimensional manifold, where potential outcomes depend in a complex way on the average intensity of light and the label of an image. The treatment also uses this one-dimensional summary, ϕ , together with an additional (hidden) synthetic confounder, U (we consider this hidden confounder as another observed covariate). HC-MNIST is then defined by the following data-generating mechanism:

$$\begin{cases} U \sim \text{Bern}(0.5), \\ X \sim \text{MNIST-image}(\cdot), \\ \phi := \left(\text{clip}\left(\frac{\mu_{N_x} - \mu_c}{\sigma_c}; -1.4, 1.4\right) - \text{Min}_c\right) \frac{\text{Max}_c - \text{Min}_c}{1.4 - (-1.4)}, \\ \alpha(\phi; \Gamma^*) := \frac{1}{\Gamma^* \text{sigmoid}(0.75\phi + 0.5)} + 1 - \frac{1}{\Gamma^*}, \\ \beta(\phi; \Gamma^*) := \frac{\Gamma^*}{\text{sigmoid}(0.75\phi + 0.5)} + 1 - \Gamma^*, \\ A \sim \text{Bern}\left(\frac{u}{\alpha(\phi; \Gamma^*)} + \frac{1-u}{\beta(\phi; \Gamma^*)}\right), \\ Y \sim N((2A - 1)\phi + (2A - 1) - 2 \sin(2(2A - 1)\phi) - 2(2U - 1)(1 + 0.5\phi), 1), \end{cases} \quad (31)$$

where c is a label of the digit from the sampled image X ; μ_{N_x} is the average intensity of the sampled image; μ_c and σ_c are the mean and standard deviation of the average intensities of the images with the label c ; and $\text{Min}_c = -2 + \frac{4}{10}c$, $\text{Max}_c = -2 + \frac{4}{10}(c + 1)$. The parameter Γ^* defines what factor influences the treatment assignment to a larger extent, i.e., the additional confounder or the one-dimensional summary. We set $\Gamma^* = \exp(1)$. For further details, we refer to (Jesson et al., 2021).

E ADDITIONAL RESULTS

E.1 PRECISION IN ESTIMATING TREATMENT EFFECT

In the following, we report results on the root precision in estimating treatment effect (rPEHE) for the baseline representation learning CATE estimators. The rPEHE is given by $\sqrt{\frac{1}{n} \sum_{i=1}^n \left((y_i[1] - y_i[0]) - \widehat{\tau}^\phi(\Phi(x_i)) \right)^2}$, where $y_i[0], y_i[1]$ are sample from both potential outcomes. Tables 6, 7, and 8 report the results for synthetic data, IHDP100 dataset, and HC-MNIST dataset, respectively. For comparison, we also provide the performance of oracle estimators, i.e., ground-truth CATE. Notably, there is no universally best method among all of the benchmarks.

Table 6: Results for synthetic experiments. Reported: in-sample and out-sample rPEHE; mean over 10 runs.

d_ϕ	rPEHE _{in}							
	1				2			
n_{train}	500	1000	5000	10000	500	1000	5000	10000
<i>k</i> -NN	0.54 ± 0.03	0.51 ± 0.02	0.48 ± 0.01	0.47 ± 0.01	0.54 ± 0.03	0.51 ± 0.02	0.48 ± 0.01	0.47 ± 0.01
BART	0.64 ± 0.04	0.60 ± 0.03	0.51 ± 0.01	0.48 ± 0.01	0.64 ± 0.04	0.60 ± 0.03	0.51 ± 0.01	0.48 ± 0.01
C-Forest	0.67 ± 0.04	<u>0.59 ± 0.03</u>	<u>0.49 ± 0.01</u>	<u>0.48 ± 0.00</u>	0.67 ± 0.04	0.59 ± 0.03	<u>0.49 ± 0.01</u>	<u>0.48 ± 0.00</u>
TARNet	0.96 ± 0.05	0.90 ± 0.07	0.90 ± 0.07	0.91 ± 0.05	0.59 ± 0.10	0.58 ± 0.06	0.55 ± 0.05	0.56 ± 0.04
BNN (MMD; $\alpha = 0.1$)	0.98 ± 0.05	0.98 ± 0.06	0.97 ± 0.01	0.97 ± 0.01	0.70 ± 0.11	0.64 ± 0.11	0.63 ± 0.08	0.59 ± 0.09
CFR (MMD; $\alpha = 0.1$)	0.96 ± 0.05	0.97 ± 0.05	0.93 ± 0.05	0.95 ± 0.01	0.61 ± 0.06	0.61 ± 0.08	0.61 ± 0.06	0.59 ± 0.09
CFR (MMD; $\alpha = 0.5$)	0.97 ± 0.05	0.98 ± 0.06	0.97 ± 0.01	0.97 ± 0.01	0.66 ± 0.07	0.72 ± 0.07	0.66 ± 0.10	0.67 ± 0.07
CFR (WM; $\alpha = 1.0$)	0.95 ± 0.04	0.97 ± 0.06	0.95 ± 0.01	0.95 ± 0.01	<u>0.56 ± 0.05</u>	0.57 ± 0.06	0.60 ± 0.08	0.53 ± 0.03
CFR (WM; $\alpha = 2.0$)	0.95 ± 0.05	0.96 ± 0.05	0.97 ± 0.04	0.96 ± 0.01	0.58 ± 0.06	0.61 ± 0.06	0.58 ± 0.08	0.57 ± 0.07
InvTARNet	0.90 ± 0.05	0.90 ± 0.07	0.87 ± 0.05	0.88 ± 0.06	0.54 ± 0.05	0.51 ± 0.03	0.51 ± 0.04	0.49 ± 0.01
RCFR (WM; $\alpha = 1.0$)	0.97 ± 0.06	0.97 ± 0.05	0.96 ± 0.01	0.95 ± 0.03	0.57 ± 0.05	0.55 ± 0.03	0.55 ± 0.03	0.55 ± 0.05
CFR-ISW (WM; $\alpha = 1.0$)	0.96 ± 0.04	0.97 ± 0.05	0.99 ± 0.10	0.96 ± 0.01	0.54 ± 0.03	<u>0.52 ± 0.02</u>	0.53 ± 0.03	0.55 ± 0.02
BWCFR (WM; $\alpha = 1.0$)	0.97 ± 0.04	0.96 ± 0.06	0.95 ± 0.03	0.95 ± 0.02	0.58 ± 0.10	0.54 ± 0.03	0.53 ± 0.02	0.51 ± 0.02
Oracle	0.457							

Lower = better (best in bold, second best underlined)
Results for *k*-NN, BART, and C-Forest are duplicated for different d_ϕ

d_ϕ	rPEHE _{out}							
	1				2			
n_{train}	500	1000	5000	10000	500	1000	5000	10000
<i>k</i> -NN	0.57 ± 0.03	0.55 ± 0.03	0.51 ± 0.01	0.51 ± 0.02	0.57 ± 0.03	0.55 ± 0.03	0.51 ± 0.01	0.51 ± 0.02
BART	0.64 ± 0.03	0.62 ± 0.04	0.52 ± 0.02	0.50 ± 0.02	0.64 ± 0.03	0.62 ± 0.04	0.52 ± 0.02	0.50 ± 0.02
C-Forest	0.68 ± 0.03	<u>0.61 ± 0.03</u>	0.51 ± 0.02	0.49 ± 0.01	0.68 ± 0.03	0.61 ± 0.03	0.51 ± 0.02	0.49 ± 0.01
TARNet	0.95 ± 0.03	0.91 ± 0.07	0.89 ± 0.08	0.92 ± 0.05	0.59 ± 0.11	0.59 ± 0.07	0.55 ± 0.05	0.57 ± 0.04
BNN (MMD; $\alpha = 0.1$)	0.97 ± 0.03	0.98 ± 0.06	0.98 ± 0.02	0.98 ± 0.03	0.70 ± 0.10	0.65 ± 0.11	0.64 ± 0.08	0.60 ± 0.09
CFR (MMD; $\alpha = 0.1$)	0.95 ± 0.03	0.97 ± 0.05	0.93 ± 0.06	0.96 ± 0.02	0.62 ± 0.07	0.62 ± 0.08	0.62 ± 0.06	0.59 ± 0.08
CFR (MMD; $\alpha = 0.5$)	0.96 ± 0.03	0.99 ± 0.04	0.97 ± 0.02	0.98 ± 0.02	0.66 ± 0.08	0.72 ± 0.07	0.67 ± 0.09	0.67 ± 0.08
CFR (WM; $\alpha = 1.0$)	0.95 ± 0.03	0.97 ± 0.05	0.95 ± 0.02	0.95 ± 0.02	0.56 ± 0.05	0.57 ± 0.06	0.61 ± 0.08	0.54 ± 0.04
CFR (WM; $\alpha = 2.0$)	0.95 ± 0.03	0.97 ± 0.05	0.97 ± 0.05	0.97 ± 0.02	0.58 ± 0.07	0.61 ± 0.06	0.58 ± 0.09	0.57 ± 0.07
InvTARNet	0.89 ± 0.04	0.90 ± 0.06	0.87 ± 0.05	0.89 ± 0.06	0.53 ± 0.04	0.52 ± 0.03	0.51 ± 0.03	<u>0.50 ± 0.02</u>
RCFR (WM; $\alpha = 1.0$)	0.96 ± 0.04	0.98 ± 0.07	0.96 ± 0.03	0.96 ± 0.03	0.57 ± 0.04	0.55 ± 0.04	0.56 ± 0.03	0.56 ± 0.04
CFR-ISW (WM; $\alpha = 1.0$)	0.96 ± 0.03	0.97 ± 0.05	1.00 ± 0.10	0.97 ± 0.02	<u>0.54 ± 0.04</u>	<u>0.53 ± 0.02</u>	0.53 ± 0.03	0.55 ± 0.02
BWCFR (WM; $\alpha = 1.0$)	0.96 ± 0.04	0.96 ± 0.05	0.96 ± 0.04	0.95 ± 0.03	0.58 ± 0.10	0.54 ± 0.04	0.53 ± 0.03	0.52 ± 0.03
Oracle	0.457							

Lower = better (best in bold, second best underlined)
Results for *k*-NN, BART, and C-Forest are duplicated for different d_ϕ

Table 7: Results for IHDP100 experiments. Reported: in-sample and out-sample rPEHE; mean over 100 train/test splits.

d_ϕ	rPEHE _{in}				
	5	10	15	20	25
k -NN	0.668 ± 0.064	0.668 ± 0.064	0.668 ± 0.064	0.668 ± 0.064	0.668 ± 0.064
BART	0.594 ± 0.124	0.594 ± 0.124	0.594 ± 0.124	0.594 ± 0.124	0.594 ± 0.124
C-Forest	0.641 ± 0.066	0.641 ± 0.066	0.641 ± 0.066	0.641 ± 0.066	0.641 ± 0.066
TARNet	0.514 ± 0.245	0.503 ± 0.235	0.502 ± 0.236	0.505 ± 0.232	0.503 ± 0.234
BNN (MMD; $\alpha = 0.1$)	0.495 ± 0.172	0.490 ± 0.175	0.500 ± 0.173	0.498 ± 0.172	<u>0.469 ± 0.184</u>
CFR (MMD; $\alpha = 0.1$)	0.463 ± 0.186	0.470 ± 0.191	0.477 ± 0.181	0.469 ± 0.188	0.476 ± 0.183
CFR (MMD; $\alpha = 0.5$)	0.462 ± 0.185	0.489 ± 0.190	0.503 ± 0.185	0.492 ± 0.176	0.500 ± 0.185
CFR (WM; $\alpha = 1.0$)	<u>0.463 ± 0.190</u>	0.465 ± 0.195	<u>0.467 ± 0.190</u>	0.466 ± 0.192	0.466 ± 0.194
CFR (WM; $\alpha = 2.0$)	0.471 ± 0.183	0.473 ± 0.191	<u>0.475 ± 0.189</u>	0.471 ± 0.191	0.471 ± 0.188
InvTARNet	0.505 ± 0.258	0.537 ± 0.310	0.523 ± 0.240	0.514 ± 0.235	0.505 ± 0.226
RCFR (WM; $\alpha = 1.0$)	0.560 ± 0.154	0.572 ± 0.147	0.499 ± 0.233	0.653 ± 0.253	0.506 ± 0.205
CFR-ISW (WM; $\alpha = 1.0$)	0.466 ± 0.183	<u>0.469 ± 0.189</u>	0.464 ± 0.195	0.466 ± 0.195	0.471 ± 0.199
BWCFR (WM; $\alpha = 1.0$)	0.581 ± 0.163	<u>0.600 ± 0.166</u>	0.599 ± 0.175	0.595 ± 0.204	0.789 ± 1.721
Oracle	0.425				

Lower = better (best in bold, second best underlined)

Results for k -NN, BART, and C-Forest are duplicated for different d_ϕ

d_ϕ	rPEHE _{out}				
	5	10	15	20	25
k -NN	0.756 ± 0.123	0.756 ± 0.123	0.756 ± 0.123	0.756 ± 0.123	0.756 ± 0.123
BART	0.615 ± 0.133	0.615 ± 0.133	0.615 ± 0.133	0.615 ± 0.133	0.615 ± 0.133
C-Forest	0.667 ± 0.123	0.667 ± 0.123	0.667 ± 0.123	0.667 ± 0.123	0.667 ± 0.123
TARNet	0.620 ± 0.292	0.622 ± 0.288	0.620 ± 0.291	0.613 ± 0.285	0.613 ± 0.285
BNN (MMD; $\alpha = 0.1$)	0.514 ± 0.181	0.510 ± 0.185	0.517 ± 0.183	0.515 ± 0.181	0.496 ± 0.195
CFR (MMD; $\alpha = 0.1$)	0.492 ± 0.193	<u>0.497 ± 0.201</u>	0.500 ± 0.186	0.493 ± 0.191	0.500 ± 0.190
CFR (MMD; $\alpha = 0.5$)	<u>0.493 ± 0.191</u>	<u>0.502 ± 0.191</u>	0.515 ± 0.191	0.509 ± 0.185	0.511 ± 0.187
CFR (WM; $\alpha = 1.0$)	0.499 ± 0.202	0.500 ± 0.211	0.495 ± 0.203	0.497 ± 0.204	0.498 ± 0.204
CFR (WM; $\alpha = 2.0$)	0.500 ± 0.198	0.496 ± 0.201	0.503 ± 0.202	0.499 ± 0.203	0.500 ± 0.196
InvTARNet	0.563 ± 0.269	0.610 ± 0.350	0.618 ± 0.287	0.605 ± 0.277	0.595 ± 0.267
RCFR (WM; $\alpha = 1.0$)	0.601 ± 0.202	0.612 ± 0.198	0.535 ± 0.228	0.676 ± 0.281	0.580 ± 0.256
CFR-ISW (WM; $\alpha = 1.0$)	0.501 ± 0.195	0.501 ± 0.203	0.496 ± 0.207	0.497 ± 0.208	0.495 ± 0.210
BWCFR (WM; $\alpha = 1.0$)	0.599 ± 0.182	0.618 ± 0.190	0.604 ± 0.184	0.601 ± 0.190	0.731 ± 0.988
Oracle	0.424				

Lower = better (best in bold, second best underlined)

Results for k -NN, BART, and C-Forest are duplicated for different d_ϕ

Table 8: Results for HC-MNIST experiments. Reported: in-sample and out-sample rPEHE; mean over 10 runs.

d_ϕ	rPEHE _{in}			rPEHE _{out}		
	7	39	78	7	39	78
k -NN	1.06 ± 0.01	1.06 ± 0.01	1.06 ± 0.01	1.10 ± 0.01	1.10 ± 0.01	1.10 ± 0.01
BART	0.89 ± 0.24	0.89 ± 0.24	0.89 ± 0.24	0.89 ± 0.25	0.89 ± 0.25	0.89 ± 0.25
C-Forest	0.82 ± 0.00	0.82 ± 0.00	0.82 ± 0.00	0.82 ± 0.00	0.82 ± 0.00	0.82 ± 0.00
TARNet	0.71 ± 0.02	0.66 ± 0.01	0.67 ± 0.03	0.72 ± 0.02	0.70 ± 0.01	0.71 ± 0.02
BNN (MMD; $\alpha = 0.1$)	0.75 ± 0.03	0.73 ± 0.03	0.93 ± 0.14	0.77 ± 0.03	0.74 ± 0.03	0.93 ± 0.14
CFR (MMD; $\alpha = 0.1$)	<u>0.73 ± 0.03</u>	<u>0.67 ± 0.01</u>	<u>0.69 ± 0.03</u>	<u>0.74 ± 0.02</u>	<u>0.71 ± 0.01</u>	<u>0.73 ± 0.02</u>
CFR (MMD; $\alpha = 0.5$)	0.86 ± 0.23	0.74 ± 0.02	0.80 ± 0.15	0.86 ± 0.13	0.76 ± 0.02	0.78 ± 0.05
CFR (WM; $\alpha = 1.0$)	1.10 ± 0.17	1.21 ± 0.14	1.37 ± 0.23	1.10 ± 0.17	1.19 ± 0.14	1.28 ± 0.14
CFR (WM; $\alpha = 2.0$)	1.40 ± 0.31	1.33 ± 0.09	1.30 ± 0.05	1.28 ± 0.10	1.30 ± 0.06	1.29 ± 0.06
InvTARNet	0.77 ± 0.05	0.69 ± 0.04	<u>0.69 ± 0.05</u>	0.76 ± 0.03	<u>0.71 ± 0.01</u>	0.71 ± 0.01
RCFR (WM; $\alpha = 1.0$)	1.83 ± 1.48	2.78 ± 4.05	3.68 ± 3.43	1.24 ± 0.29	2.66 ± 4.33	3.05 ± 3.72
CFR-ISW (WM; $\alpha = 1.0$)	1.29 ± 0.12	1.25 ± 0.04	1.28 ± 0.06	1.25 ± 0.05	1.26 ± 0.08	1.27 ± 0.07
BWCFR (WM; $\alpha = 1.0$)	2.92 ± 2.39	1.31 ± 0.05	1.35 ± 0.05	1.46 ± 0.45	1.32 ± 0.06	1.35 ± 0.05
Oracle	0.522			0.513		

Lower = better (best in bold, second best underlined)

Results for k -NN, BART, and C-Forest are duplicated for different d_ϕ

E.2 POLICY ERROR RATES AND DEFERRAL RATES

Here, we examine the trade-off between the improvement in the error rates and the increase in the deferral rates, which appear after the application of our refutation framework. One way to do so is through *policy error rate vs. deferral rate* plots, as in (Jesson et al., 2021). In Figures 4, 5, and 6, we report the error rates and the deferral rates for synthetic data, IHDP100 dataset, and HC-MNIST dataset, respectively. Therein, the baseline representation learning methods for CATE are shown as points located at the vertical line with a deferral rate of zero. Each of those points is then connected with a point corresponding to our bounds performance. As a result, we see that our refutation framework achieves an improvement in the error rates with only a marginal increase in the deferral rates.

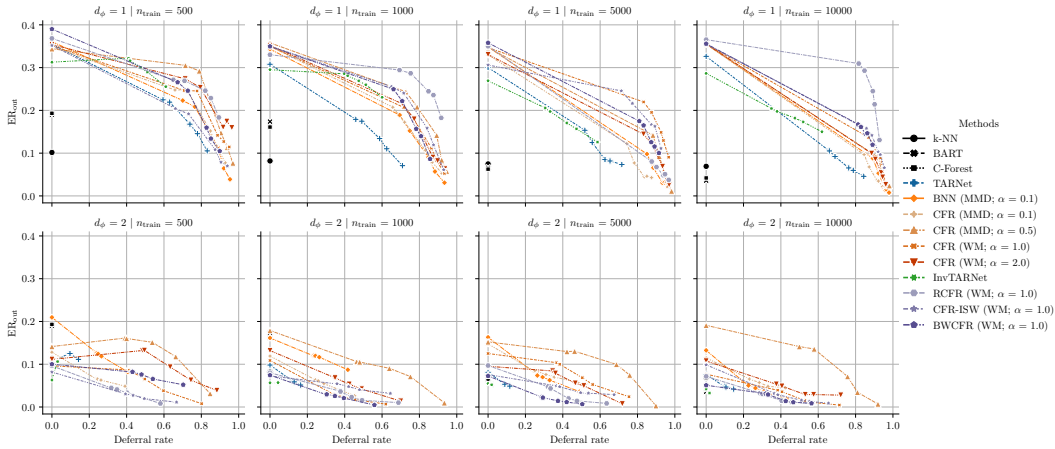


Figure 4: Policy error rate vs. deferral rate plot for synthetic data. Reported: out-sample performance of baseline methods connected with the performance of our refutation framework; mean over 10 runs. Here, δ varies in the range $\{0.0005, 0.001, 0.005, 0.01, 0.05\}$, which corresponds to several scatter points per line.

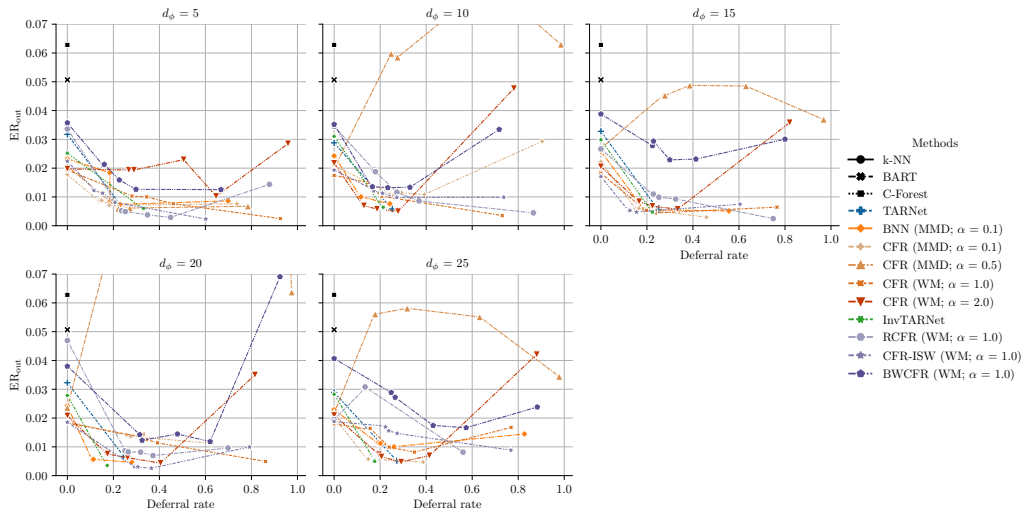


Figure 5: Policy error rate vs. deferral rate plot for IHDP100 dataset. Reported: out-sample performance of baseline methods connected with the performance of our refutation framework; mean over 100 train/test splits. Here, δ varies in the range $\{0.0005, 0.001, 0.005, 0.01, 0.05\}$, which corresponds to several scatter points per line.

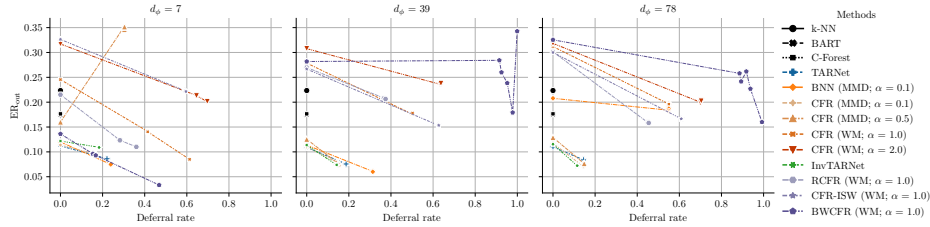


Figure 6: Policy error rate vs. deferral rate plot for HC-MNIST dataset. Reported: out-sample performance of baseline methods connected with the performance of our refutation framework; mean over 10 runs. Here, δ varies in the range $\{0.0005, 0.001, 0.005, 0.01, 0.05\}$, which corresponds to several scatter points per line.

E.3 DECISION BOUNDARIES

In Fig. 7 and 8, we provide plots of the decision boundaries for all the baselines (using the synthetic benchmark). Therein, we plot both the ground-truth boundaries and boundaries, estimated with our refutation framework in combination with different representation learning methods for CATE. On the left side ($d_\phi = 1$), the low-dimensional representation induces at the same time loss of heterogeneity and confounding bias. We see that our bounds remain approximately valid for CATE wrt. representations, even when the dimensionality of the representation is misspecified, especially for different variants of CFR and InvTARNet. On the right side ($d_\phi = 2$), there is no loss of heterogeneity but still some hidden confounding induced. Yet, our bounds are valid for both CATE wrt. representations and covariates for all the baselines. Additionally, we observe that the tightness of the estimated bounds highly depends on the representation learning baseline, e. g., the bounds on the RICB are the tightest for InvTARNet, as its representations introduce almost no confounding bias.

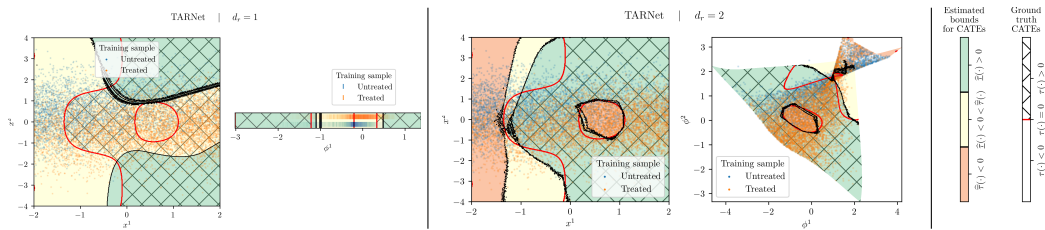


Figure 7: Decision boundaries for the synthetic dataset. Ground-truth and estimated boundaries are shown with hatches and colors, respectively. Training samples ($n_{\text{train}} = 10,000$) are shown too to highlight treatment imbalance. Here, $\delta = 0.01$.

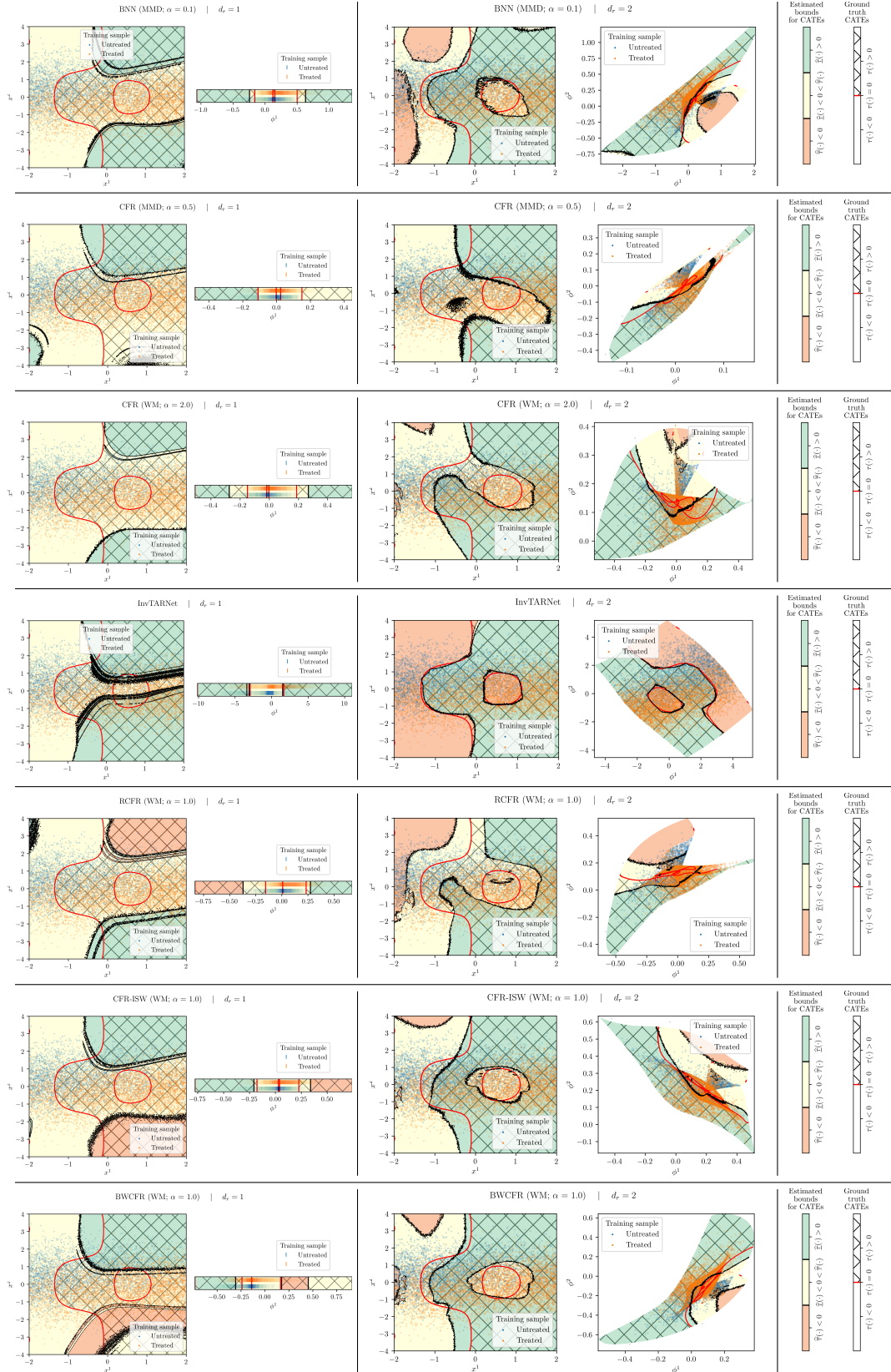


Figure 8: Decision boundaries for the synthetic dataset. Ground-truth and estimated boundaries are shown with hatches and colors, respectively. Training samples ($n_{\text{train}} = 10,000$) are shown too to highlight treatment imbalance. Here, $\delta = 0.01$.